Published in Palaeogeography, Palaeoclimatology, Palaeoecology 521 (2019) 10–29

Palaeoenvironmental changes during the late Albian oceanic anoxic event 1d: An example from the Capacho Formation, southwestern Venezuela

María-Emilia Rodríguez-Cuicas [1,2], Jean-Carlos Montero-Serrano[2,3*], Grony Garbán[1,4]

[1] *Instituto de Ciencias de la Tierra, Universidad Central de Venezuela, 3895, Caracas 1010-A, Venezuela*

[2]*Institut des sciences de la mer de Rimouski, Université du Québec, à Rimouski, 310 allée des Ursulines, Rimouski, Quebec G5L 3A1, Canada*

[3]*GEOTOP Research Center, C.P. 8888, succursale centre-ville, Montreal, Quebec H3C 3P8, Canada*

[4]*DTP Laboratorios SRL, Condarco 1136, Buenos Aires, Argentina.*

*Corresponding autor: Phone: +1.418.723.1986 Ext: 1139; Fax: +1.418.724.1842.

E-mail addresses: memilia.rc@gmail.com (M.-E. Rodríguez-Cuicas), jeancarlos_monteroserrano@uqar.ca (J.-C. Montero-Serrano), gjgarban@gmail.com (G. Garban).

Abstract

The late Albian–early Cenomanian oceanic anoxic event 1d (OAE-1d; ~ 103 to 99.5 Ma) represents a global interval of enhanced organic carbon burial due to widespread oxygen deficiency in the water column and/or increased primary productivity. The biostratigraphy and geochemistry of organic-rich sediments in the La Grita Member (Capacho Formation) in southwestern Venezuela were studied to document the paleoenvironmental conditions that governed the deposition of this succession during OAE-1d. Carbon-isotope ($\delta^{13}C_{carb}$ and $\delta^{13}C_{Corg}$) chemostratigraphy and biostratigraphic constraints show that the La Grita Member spans the late Aptian period (*Rotalipora appenninica* Zone), and that OAE-1d is well recorded in this succession. A prominent increase in total organic carbon (TOC) values (up to 10%) is clearly recorded through the onset of OAE-1d, coinciding with a prominent change in

overall redox-sensitive proxies suggesting that the La Grita Member sediments accumulated under anoxic (and possibly euxinic) bottom-water conditions in a partially restricted basin. The detrital proxies suggest that the greenhouse climate prevailing during OAE-1d induced significant acceleration of the hydrologic cycle and an increase in continental chemical weathering rates. Overall, the carbon and oxygen isotope records, TOC contents, as well as the detrital proxies show cyclic variation during the late Albian stage. These variations support the hypothesis that orbital forcing likely also modulated the equatorial monsoonal activity during the OAE-1d.

Keywords: Mid-Cretaceous**;** Sedimentary geochemistry; Stable isotopes; Biostratigraphy; Paleoenvironment; Redox conditions.

1. Introduction

The mid-Cretaceous (i.e., Albian–Turonian; 110–90 Ma) is an interval in which an increase in the production of oceanic crust, together with the formation of large igneous provinces, promoted pCO_2 emission to the atmosphere and the conjunction of a greenhouse climate (Arthur et al., 1985; Barron and Washington, 1985; Leckie, 2002; Bodin et al., 2015). As a consequence, high temperatures and the acceleration of the hydrological cycle (Menegatti et al., 1998; Bodin et al., 2015) led to increased primary productivity causing anoxic oceanic conditions (Föllmi et al., 1994; Turgeon and Brumsack, 2006) and producing several distinctive episodes of organic matter accumulation called oceanic anoxic events (OAEs; Jenkyns, 1980). Since such events disturb the carbon cycle, carbon isotope stratigraphy is traditionally used as a marker to recognize oceanic anoxic events (Sholle and Arthur, 1980; Herrle et al., 2004; Jenkyns, 2010).

53 Most studies of OAEs occurring in the mid Cretaceous have focused on OAE-1a
54 (e.g., Erba, 1994; Menegatti et al., 1998) and on OAE-2 (e.g., Arthur et al., 1987;
55 Gale et al., 1993; Huber et al., 2002). However, less research has been carried out on
56 sub-OAEs such as OAE 1b and 1d because they represent occurrences of organic-rich
57 black shale that are less thick, rather patchy in distribution, and less pronounced
58 isotopic records (e.g., Robinson et al., 2004; Navarro-Ramirez et al., 2015). Unlike
59 the main OAEs of the Mesozoic era (Jenkyns, 2010), OAE-1d is characterized by a
60 moderate (0.5 to 2‰) positive carbon isotope ($\delta^{13}C$) excursion (Wilson and Norris,
61 2001; Bornemann et al., 2005; Watkins et al., 2005; Meyers et al., 2006; Gambacorta,
62 2011; Giorgioni et al., 2012). Thus, coupling carbon isotope with inorganic
63 geochemical proxies could help in the reconstruction of depositional conditions and
64 highlights the occurrence of OAE events when traditional signals may not be as
65 apparent (Erbacher et al., 1999; Scott et al., 2013).
66 The study of OAE-1d has gained importance thanks to the studies of Wilson and
67 Norris (2001), which showed that the "Breistroffer" event (or OAE-1d) was a global
68 event that was the product of the collapse of the stratification of the upper ocean, at
69 least in western tropical Atlantic. More recently, some authors have suggested that
70 OAE-1d was triggered by a period of enhanced orbital forcing, which induced an
71 exceptionally strong seasonal contrast, with resulting unstable circulation that favored
72 the expansion of deep-water anoxic conditions (Bornemann et al., 2005; Giorgioni et
73 al., 2012; Giorgioni et al., 2015).
74 The rocks deposited during the Cretaceous in western Venezuela reflect the
75 combination of different factors, such as relative changes in sea level, the occurrence
76 of OAEs, upwelling currents, and restricted circulation, which are intimately linked to
77 the paleoceanographic, bathymetric characteristics, and climate (Macellari, 1988;

Pérez-Infante et al., 1996; Villamil et al., 1999; Erlich et al., 1999a,b). Some of these Cretaceous units have been well correlated with global events, such as the OAE-1a and 1b events represented by the Cogollo Group (Méndez-Dot et al., 2015), and the OAE-2 (Cenomanian-Turonian) represented mainly by the La Luna Formation (Tribovillard et al., 1991; Pérez-Infante et al., 1996; Erlich et al., 1999a,b). The La Grita Member in the Capacho Formation (southwestern Venezuela) is characterized by anoxic facies, dense black limestones intercalated with marly limestones of Albian–Cenomanian age (Renz, 1959). However, there have been no detailed biostratigraphic and geochemical studies documenting the paleoenvironmental sedimentation conditions of this succession, the precise calibration of their age, and their possible correlation with globally recorded anoxic Cretaceous events. Therefore, using biostratigraphic and geochemical tools (such as stable isotope analysis and elemental geochemistry), this work aims not only to investigate the expression of OAE-1d in northwestern South America, but also to better document the main impacts of this event in the depositional environment in the La Grita Member.

2. Geological setting

2.1. Cretaceous stratigraphy of western Venezuela

During the Cretaceous, the western margin of South America was covered by various transgressive cycles, favouring the deposition of rocks of huge economic importance due to their hydrocarbon contents (Macellari, 1988; Erlich et al., 1999a,b). The Mesozoic–Cenozoic stratigraphy sequence established for western Venezuela is a result of the interaction of tectonic and thermal subsidence, variations in sediment sources, and changes in global sea level (Macellari, 1988; Pindell, 1993; Parnaud et al., 1995; Lugo and Mann, 1995). The Pangea Jurassic rifting stage caused various

significant tectonic events that subsequently influenced the evolution of the sedimentary basins. The opening of the Proto-Caribbean caused graben formation (e.g., the Andes, Perijá, and Lake Maracaibo), which were then filled during the Jurassic by lacustrine, fluvial, and volcanic sediments. From the early to late Cretaceous (Fig. 1), the region shifted to a passive continental margin stage, and sedimentation was largely controlled by the Jurassic graben system (González de Juana et al., 1980; Pindell, 1985), evidenced in the sandy lithology of the Río Negro Formation. Subsequently, the subsidence stabilized and the Cogollo group (Apón, Lisure, Maraca successions) was deposited in an extensive epicontinental sea. During the Cenomanian-Santonian the maximum marine cover was deposited, forming the anoxic-euxinic environments that gave rise to the deposition of the Capacho and La Luna formations. After maximum transgression, a regressive cycle began that conserved the marine environment and is evidenced by the glauconitic and phosphatic layers of the Tres Esquinas Member in the La Luna Formation. Finally, the shales of the Colón Formation were deposited, which change transitionally to the Mito Juan Formation (Fig. 2A; González de Juana et al., 1980; Parnaud et al., 1995)

According to Villamil and Pindell (1998), the middle–late Albian stratigraphic record west of Venezuela shows an abrupt transgression generating regional condensed sediments and the deposition of significant intervals of source rocks. The upper condensed transgressive systems tract (late Albian) is characterized by the deposition of the La Grita Member facies in the Capacho Formation in western Venezuela, as shown in terms of sequence stratigraphy in Figure 2D. This deposition cycle began with basal transgressive sand from the early to late Albian, corresponding to the Aguardiente Formation (sandstone and silstone). This formation represents a tidal-dominated deltaic system (Renz, 1959; Maceralli, 1988) and is stratigraphically

a highstand systems tract (HST). With the progressive increase in sea level, the La Grita Member represents a transgressive systems tract (TST) characterized by anoxic facies in which the unit top represents the maximum flooding surface (MFS) (Macellari, 1988; Méndez et al., 2015). The final phase of the cycle is represented by shales at the base of the Seboruco Member (Renz, 1959). Towards the southeast of the basin, the La Grita Member changes transitionally to the basal shales of the Ecandalosa Formation, while in the northeast the member passes transitionally to the base of the La Luna Formation (Renz, 1959; Fig. 2B)

The La Grita Member is 5–10 m thick, with a lithology very similar to the calcareous shales facies of the La Luna Formation, which are dense black limestones finely intercalated with black to dark-grey calcareous shales and calcareous concretions. Overall, the petrographic study by Rodríguez (1989) classifies these rocks as mudstone and wackestone (Dunham, 1962). In more detail, the limestones are typified by high contents in organic matter, pyrite, and a dark micritic matrix that is partially recrystallized (microspar-pseudospar). The matrix contains microfossils (mainly planktonic foraminifera), quartz, and accessory minerals such as fluorapatite, glauconite, muscovite, and zircon.

2.2. Occurrence of Cretaceous oceanic anoxic events in western Venezuela

The conditions of anoxia and the intervals of high content of organic matter recorded in western Venezuela during the Cretaceous have been correlated chronostratigraphically to different OAEs represented in the Aptian (OAE-1a and 1b; Baquero et al., 2008; Mendez et al., 2008; Mendez-Dot et al., 2015), Cenomanian-Turonian (OAE-2; Pérez-Infante et al., 1996; Erlich et al., 1999a), and Coniacian-Santonian (regional OAE-3; Rey et al., 2004; Machado et al., 2016).

Baquero et al. (2008) have described two major transgressive events in the Apón Formation, which correspond to the Machiques Member (OAE-1a; early Aptian) and the top of the Piché Member (OAE-1b; late Aptian). Both levels have an average TOC between 2-3%, with occasional values between 5-6% (Méndez et al., 2008). The Machiques Member is a pelagic limestone originated on the shallow platform, interspersed with some transgressive events that moved from pelagic to the shallow-water platform facies (Méndez et al., 2008). The Piché Member is a stratigraphic transgressive and regressive sequence. Towards the top of this member the anoxic environments were transferred to the internal platform by marine transgressions as happened in the Machiques Member. Based on the stratigraphic distributions of trace metals (Mo, V, Fe) and sulfur in the Aptian-Albian interval of the Machiques Member, Alberdi and Tocco (1999) suggest deposition conditions with cyclic pattern of oxic-anoxic episodes and the deposit of a mixture of marine and terrestrial organic matter.

On the other hand, the La Luna Formation represents the most important source rock of the region with average TOC values of ~6% (Talukdar et al., 1985; Talukdar and Marcano, 1994). The highest TOC intervals occur across the Cenomanian-Turonian, Coniacian-early Santonian, and rapidly decrease during the late Santonian (Erlich et al., 1999b). In the La Luna Formation the accumulation of organic matter began in the middle to late Cenomanian in an open marine environment, with depths of a few hundred meters and very low clastic contribution. Pérez-Infante et al. (1996) suggest that this black shale deposition from the La Luna Formation was a local response to the conjunction of an increase in sea level and the presence of upwelling currents. The Cenomanian/Turonian boundary event is marked in the middle section of the La Luna Formation with a positive change in $\delta^{13}C_{org}$ values, which does not

177 respond to local changes in bioproductivity or in the intensification of anoxic
178 conditions (Pérez-Infante et al. al., 1996), therefore possibly marks the global isotopic
179 change associated with OAE-2. Conversely, $\delta^{13}C_{carb}$ values in Coniacian-Santonian
180 interval not fit with the significant carbon isotope excursion as expected for the OAE
181 and support the hypothesis that OAE-3 is not a global but a regional anoxic event with
182 restricted areal distribution of organic carbon burial in the low-to-mid latitude (e.g.,
183 Wagreich, 2012; Machado et al., 2016).

184 Overall, the Maracaibo Basin represents an interesting conjunction that involves
185 hydrocarbon generating levels and levels with conventional porosities and fractures
186 that act as flow units and reservoir of hydrocarbons, forming a petroleum system of
187 economic importance (e.g., Talukdar et al., 1985; Talukdar and Marcano, 1994;
188 Méndez et al., 2015).

189

190 # 3. Material and methods

191 ## 3.1 Sampling

192 The stratigraphic section was sampled from an outcrop on the Guaruríes River
193 (8°25'08"N; 71°46'31"W; 5.3 km SW of the village of Zea) in the Tovar district, state
194 of Mérida (Fig. 2B). The La Grita Member is approximately 7 m thick in this outcrop.
195 A total of 33 samples were collected every 25 cm in the La Grita Member interval and
196 every 100 cm in the underlying units (Maraca Formation to the Aguardiente
197 Formation) and overlying unit (Seboruco Member) (Fig. 3). An aliquot (~50–100 g)
198 of each sample was crushed and ground with a tungsten carbide Shatterbox mill.
199 Later, each sample was sieved through a 100-mesh screen in order to homogenize the
200 degree of pulverization.

201

3.2 Biostratigraphic analysis

For the biostratigraphic analysis, thin sections were prepared from 14 samples chosen considering lithological changes, mineral composition, and stratigraphic level (Fig. 5). Due to the high degree of diagenesis, the foraminifera were classified by shape, chamber arrangement, and size. To determine biostratigraphic Zones and age, we used the Zone scheme of Sliter (1989) and Premoli Silva and Sliter (1995). The microfossils preserved in rocks thus identified provided data on relative age, sedimentary environment, and the paleo-ecological conditions of deposition of the La Grita Member.

3.3 Analytical procedures

3.3.1. Stable isotope analysis (carbon and oxygen)

Bulk carbonate carbon ($\delta^{13}C_{Carb}$) and oxygen ($\delta^{18}O_{carb}$) isotope analyses were carried out on powdered bulk-rock samples using a dual-inlet stable isotope mass spectrometer system (Thermo Fisher Scientific Delta Plus V). Organic carbon isotopes ($\delta^{13}C_{org}$) were also measured on the bulk organic fraction of decarbonated (6M HCl treatment) samples using a Flash EA 1112 automatic elemental analyser connected to a Thermo Fisher Scientific Delta Plus V isotope ratio mass spectrometer via a Conflo III interface. The stable carbon and oxygen isotope ratios are reported in the delta notation as the per mil (‰) deviation relative to the Vienna Pee Dee Belemnite (VPDB) standard. Analytical precision and accuracy were determined by replicate analyses of samples and replicate analyses of in-house standards (CAL-INT, acetanilide, and sucrose; Appendix A.1 and A.2), calibrated with international standards (NBS16, NBS17, NBS18, NBS19, NBS22, USG24; Appendix A.3) and were better than ±0.2‰ (1σ) for carbon and ±0.5‰ (1σ) for oxygen.

3.3.2 Total organic carbon, total sulfur and pyrite analyses

Total organic carbon (TOC) and total sulfur (S_t) was determined on the carbonate-free fraction (cff) using a LECO CS-600 elemental analyzer. The decarbonated fraction was obtained by a 6M HCl treatment. TOC contents were recalculated to the original sample mass.

The pyrite content was studied by X-ray diffraction (XRD). The random powder samples were side-loaded into the holders and analysed on a PANalytical X'Pert Powder diffractometer. This instrument is fitted with a copper tube (Cu K-alpha = 1.54178 Å), operating at 45 kV and 40 mA and a post-diffraction graphite monochromator. Samples were scanned from 5° to 65° two-theta in steps of 0.020° two-theta and a counting time of 2 seconds per step. For the semi-quantification of the major mineralogical components, bulk sediment XRD scans were processed in the software package X'Pert High-Score Plus (PANalytical) using the Rietveld full-pattern fitting method (e.g., Young, 1993; Grunsky et al., 2013). This method permits the semi-quantification of whole-sediment mineralogy with a precision of 5% for non-phyllosilicates minerals. In this article, only the pyrite content is used.

3.3.3 Analysis of major, minor, and trace elements

A total of 11 elements (Al, Si, P, K, Ca, Ti, Mn, Fe, V, Sr, Zr) were analyzed by energy dispersive X-ray fluorescence (EDXRF) spectrometry using a PANalytical Epsilon 3-XL. Before EDXRF analysis, loss on ignition (LOI) was determined gravimetrically by heating to 950°C for two hours. Subsequently, samples were treated by borate fusion in an automated fusion furnace (CLAISSE® M4 Fluxer). Samples weighing ~0.6 g were mixed with ~6 g of lithium borate flux (CLAISSE, pure, 49.75% Li2B4O7, 49.75% LiBO2, 0.5% LiBr). The mixtures were melted in Pt-Au crucibles (95% Pt, 5% Au), and after fusion the melts were cast to flat disks

(diameter: 32 mm; height: 3 mm) in Pt-Au moulds. Acquired XRF spectra were processed with the standardless Omnian software package (PANalytical). The resulting data are expressed as weight percent (wt.% ; Al, Si, P, K, Ca, Ti, Mn, Fe) and micrograms per gram (µg/g; V, Sr, Zr). Procedural blanks always accounted for less than 1% of the lowest concentration measured in the sediment samples. Analytical accuracy and precision were found to be better than 1–5% for major elements and 5–10% for the other elements, as checked by an international standard (USGS SDC-1; Appendix B.1) and analysis of replicate samples.

Further major and trace elements (e.g., Na, Sc, Cr, Ni, Cu, Zn, Rb, Nb, Mo, Hf, Th, U) were analyzed by laser ablation inductively coupled plasma mass spectrometry (LA-ICP-MS) as described in previous studies (e.g., Jackson, 2001, 2008; Leite et al., 2011; Wegner et al., 2015). A NewWave UP213 196 nm excimer ablation system interfaced to an inductively coupled plasma-quadrupole mass spectrometer (ICP-QMS Agilent 7500c) was used for the ablation of the lithium tetraborate discs previously analyzed by EDXRF. Operating conditions of the ablation system included a 10 Hz repetition rate, 100 µm spot size, 5µm.s^{-1} scanning velocity, and circa 10 J.cm^{-2} on-sample energy density. Helium was used as a carrier gas; the make-up gas argon was admixed after the ablation cell and the aerosol carried to the ICP-MS. The acquisition times for the background and the ablation interval were circa 170 and 370 s, respectively. Dwell times per isotope ranged from 10 ms for major elements to 30 ms for trace, and peak-hopping mode was employed. The ICP-MS system was tuned using a NIST SRM 612 synthetic glass standard to ensure robust plasma conditions while maximizing the signal to background intensity ratio and retaining low oxide-production levels (<0.5% ThO). Bracketed external standardization used NIST SRM 612 glass. Calcium contents obtained by EDXRF were used for internal

277 standardization. Data reduction for concentration and limit of detection calculations
278 was undertaken offline using the software LAMTRACE (Jackson, 2008). Procedural
279 blanks always accounted for less than 1% of the lowest concentration measured in the
280 samples. The analytical accuracy and precision were found to be better than 4% for all
281 elements, as checked by NIST SRM 612 (Appendix B.2) standard and analysis of
282 replicate samples.

283 The chemical index of alteration (CIA), corrected for the carbonate and phosphate
284 contents (e.g., McLennan et al., 1993; Fedo et al., 1995), was used to evaluate the
285 degree of chemical weathering in the source areas. This index was calculated as
286 follow: CIA= 100 x $[Al_2O_3/(Al_2O_3+CaO^*+Na_2O+K_2O)]$ in molar proportions (Nesbitt
287 and Young, 1982). Likewise, to compare the relative enrichment of redox-sensitive
288 elements (RSTE: V, Ni, Cr, Zn, Mo, U), we calculated enrichment factors (EF) by
289 comparing Al-normalized metal concentrations to those of average shale (Wedepohl,
290 1991): $X_{EF} = [(X/Al)_{sample}/(X/Al)_{average\ shale}]$. In practical terms, EF > 3 represents a
291 detectable authigenic enrichment of an element over average shale concentrations,
292 whereas EF > 10 represents a moderate to strong degree of authigenic enrichment
293 (e.g., Tribovillard et al., 2006).

294 A compositional Q-mode cluster analysis (e.g., Egozcue and Pawlowsky-Glahn,
295 2005; Pawlowsky-Glahn and Egozcue, 2011; Montero-Serrano et al., 2015) was
296 performed on the elemental geochemical dataset with the goal of finding elemental
297 associations with similar relative variation patterns that may be interpreted from a
298 palaeoenvironmental standpoint (e.g., Jaminski et al., 1998; Hoffman et al., 1998;
299 Reátegui et al., 2005; Montero-Serrano et al., 2010a, 2015). This analysis was carried
300 out using a log-ratio approach (Egozcue and Pawlowsky-Glahn 2005). Likewise, as a
301 measure of dissimilarity we use the variation array, and as a clustering criterion the

Ward method. All statistical calculations were conducted with "R" software using the packages "StatDA" (Reimann et al., 2008) and "compositions" (van den Boogaart and Tolosana-Delgado, 2008).

In addition, in order to infer palaeoenvironmental changes (e.g., weathering, sediment input, redox conditions) during OAE-1d, the stratigraphic distribution of the elemental geochemical associations obtained by the compositional Q-mode cluster analysis were represented as elemental balances **(1)**. Elemental balances are log-contrasts resulting from a log-ratio of two geometric means of two non-overlapping elemental groups (Egozcue and Pawlowsky-Glahn, 2005). The general expression of an elemental balance is:

$$b = [\sqrt{(r \times s / r + s)}] \times \mathrm{Log}[gm(A)/gm(B)] \qquad \textbf{(1)}$$

where A, B are two non-overlapping elemental groups of a complete composition x of D elements (e.g., Ti, Zr, Si, K, Al,…, x_D), r and s ($r + s \leq D$) are the number of elements in A, B respectively, and gm(.) denotes the geometric mean of the elemental groups A and B.

All analytical data presented are available electronically in the Supplementary Appendix B.1 and B.2.

4. Results

4.1 Biostratigraphy

Diversity is relatively low in the planktonic foraminifer assemblage in the La Grita Member, and it is dominated by the following species: *Hedbergella (delrioensis, planispira, rischi, simplex), Globigerinelloides (bentonenis, ultramicra, caseyi), Ticinella (roberti, primula, raynaudi), Heterohelix (morenami, reussi)* and, to a lesser extent, *Planomalina (buxtorfi), Whiteinella (baltica),* and *Rotalipora (ticinensis)* (Fig.

4). Note that the biostratigraphic Zones have certain limitations since the total foraminifer assemblage was not counted. The different biostratigraphic Zones characterizing the La Grita Member are described below (Fig. 5):

- *Rotalipora appenninica* Zone (late Albian). Covers the interval of samples ZEARG-185 (based on the La Grita Member) to ZEARG-95 (top of La Grita Member). This interval is characterized by the presence of the species *Ticinella primula*, *Ticinella roberti*, *Ticinella raynaudi*, *Biticinella breggiensis*, *Hedbergella rischi*, and *Planomalina* cf *praebuxtorfi*, with *Rotalipora* cf *ticinensis* identified towards the base of the sequence. Towards the top of the Zone, *Heterohelix moremani* was identified.

- *Rotalipora brotzeni-Rotalipora reicheli* Zone (early Cenomanian). The microphotographs show no evidence of an early Cenomanian age from the *Rotalipora brotzeni* Zone to the *Rotalipora reicheli* Zone. Above sample ZEARG-95 (boundary of previous Zone), a thin section analysis on the sample ZEARG-90 revealed the species *Hedbergella planispira.* However, this species' wide stratigraphic range does not aid in constraining the age for this interval.

- *Rotalipora cushmani* Zone (late Cenomanian). At the top of this sequence (from sample ZEARG-85 to ZEARG-05), the foraminifer assemblage is characterized mainly by species from the genera *Hedbergella*, *Globigerinelloides*, and *Heterohelix*. The first occurrence of *Heterohelix reussi* in sample ZEARG-85 and the presence of *Whiteinella* cf *baltica* in sample ZEARG-65 identify it as a *Rotalipora cushmani* Zone.

4.2. Stable isotopes ($\delta^{13}C_{Carb}$, $\delta^{18}O_{Carb}$, $\delta^{13}C_{org}$), total organic carbon and pyrite

The vertical distributions of $\delta^{13}C_{carb}$, $\delta^{18}O_{carb,}$ and $\delta^{13}C_{org}$ for the La Grita Member are presented in Figure 6A-C. Generally, $\delta^{13}C_{carb}$ trends towards more positive values upwards in the stratigraphic column. At the boundary between the Aguardiente Formation and the La Grita Member, carbon isotope values of carbonate show a pronounced positive carbon isotope excursion (or CIE) of ~4‰. Within the *Rotalipora appenninica* Zone, corresponding to OAE-1d the magnitude of this positive CIE is around 1‰ (Fig. 6A). Within this $\delta^{13}C$ anomaly, four cyclical variations (~2.6‰ in magnitude) are observed. In contrast, the $\delta^{13}C_{carb}$ values in the Seboruco Member shows few variations, with average values of ~-1‰.

The $\delta^{18}O_{carb}$ values in the section corresponding to the Aguardiente Formation and Maraca show a shift of ~8.9‰ towards more positive values of $\delta^{18}O$ (from -14.1‰ to -5.2‰; Fig. 6B). In the interval corresponding to the La Grita Member, the $\delta^{18}O_{carb}$ profile also shows cyclical variations ranging from -12.7‰ to -10.2‰, which are significantly high values (over -5‰). The cyclical variations noted in the $\delta^{18}O_{carb}$ profile could be related to the cyclical trend observed for $\delta^{13}C_{carb}$. In contrast, the $\delta^{18}O_{carb}$ profile in the Seboruco Member shows few variations, with average values of ~ -10.6‰.

Furthermore, carbon isotope values of bulk organic matter ($\delta^{13}C_{org}$; Fig. 6C) show relatively higher values in the Aguardiente and Maraca successions (-27 to 26‰) compared to the La Grita and Seboruco members (~ -28‰). TOC concentrations are low in the Aguardiente and Maraca formations (<1%) compared to the La Grita Member and Seboruco (5-10%; Fig. 6D), while pyrite shows a slight increase during the positive CIE with two marked increases (up to 4%; Fig. 8C) recorded in the base of the La Grita Member.

4.4 Elemental geochemistry

376 The compositional Q-mode cluster analysis of the La Grita Member revealed four
377 major elemental geochemical associations (Fig. 7):
378 Redox (V, Zn, U, Mo, Cr, Ni) and organic matter-sulphide (TOC, S) groups:
379 consists of elements that tend to be less soluble or sulfide forming under reducing
380 conditions. Indeed, these elements are commonly associated with the organic matter
381 and the authigenic sulfides fraction, whose accumulation is largely controlled by the
382 oxic-anoxic conditions of the sedimentary environment (e.g., Jaminski et al., 1998;
383 Algeo and Maynard, 2004; Brumsack, 2006; Tribovillard et al., 2006; Calvert and
384 Pedersen, 2007). Among these elements, and U–Mo covariation are reputed
385 paleoredox-indices (e.g., Jones and Manning, 1994; Algeo and Maynard, 2004;
386 Tribovillard et al., 2006; Algeo and Ingall, 2007).
387 Siliciclastics group (Al, Si, Ti, K, Sc, Rb, Nb, Hf, Zr): consists of elements
388 associated with clay and silt particles, mainly as chemical constituents of the detrital
389 mineral grains (e.g., phyllosilicates, quartz, plagioclases, K-feldspar) or adsorbed on
390 their surface (e.g., Calvert and Pedersen, 2007; Montero-Serrano et al., 2010, 2015).
391 Thus, the variability of riverine inputs related to continental climate fluctuations and
392 the subsequent hydraulic partitioning of the sediments mostly control the distribution
393 and accumulation of these elements. Among these detrital elements, the Rb/Sr, Ti/Al
394 ratios may be used to evaluate detrital fluxes and changes in chemical weathering at
395 the source areas (Li et al., 2003; Croudace and Rothwell, 2015).
396 Carbonates group (Ca, Sr): consists of elements related with calcium carbonate
397 (mainly calcite) associated with calcareous cement as well as planktonic fauna
398 (including *Hedbergellas*, *Globigerinelloides*, *Ticinellas*, *Planomalinas*, *Whiteinellas*,
399 and *Rotaliporas*), which agrees with the petrographic interpretations. The carbonate-

400 associated elements correlate negatively with the other two elemental associations,
401 and thus likely represent a dilution fraction.

402 Fe-Mn oxyhydroxides group (Mn-Fe-P-Cu-Na): consists of elements mainly found
403 in the structure of Fe-Mn-oxyhydroxides. Due to the reactive nature of Fe-Mn-
404 oxyhydroxides, some other elements such as P and Cu can be sorbed on the surface of
405 this mineral phase (Delaney, 1998; Mort et al., 2007). In addition, P can also be
406 associated with organic matter, detrital material, and authigenic minerals such as
407 colophane (Mort et al., 2007) as well as skeletal remains. In fact, abundant brachiopod
408 shells and fish bones were identified in a previous petrographic study of the La Grita
409 Member (Rodríguez, 1989).

410 Based on these geochemical associations, elemental balances [$b_{(siliciclastic/carbonate)}$
411 and $b_{(redox/carbonate)}$] are performed. The vertical distribution of the siliciclastic balance
412 (Al, Si, Ti, K, Sc, Rb, Nb, Hf, Zr) and redox balance (V, Zn, U, Mo, Cr, Ni) show
413 similar patterns (Figs. 7A,D; 8G; 11A), with minimum values recorded in the
414 Aguardiente and Seboruco members and maximum values in the *Rotalipora*
415 *appenninica* Zone. Similary, detrital element ratios (Rb/Sr, Ti/Al and CIA index) also
416 increase in the *Rotalipora appenninica* Zone.

417 The stratigraphic distribution of the RSTE enrichment factors (U, V, Mo, Cr, Ni,
418 and Zn) is show in Figure 8A-B. In general, these elements record heavy enrichment
419 only at the base and top of the La Grita Member, with values ranging between 10 to
420 100 (some up to 500) times in comparison to average shale.

421

422 ## 5. Discussion

423 ### 5.1 Biostratigraphy and age of the La Grita Member

The studied foraminifer assemblages show that the La Grita Member is located in the *Rotalipora apenninica* Zone, which is indicative of a range of ages between 100.1–98.9 Ma (Premoli Silva and Verga, 2004). In addition, the absence of marker foraminifer species from the early Cenomanian (zones *Rotalipora brotzeni* and *Rotalipora reicheli*) suggest this time interval is likely condensed in a limestone bed at a stratigraphic depth of 8.25 m (~25 cm thick). However, in agreement with several sedimentological studies from western Venezuela (Canache et al., 1994; Crespo et al., 1999; Truskowski, 2006), we attribute this to the presence of a stratigraphic gap or hiatus covering the early Cenomanian interval. Indeed, Canache et al. (1994) suggest this hiatus is related to the collision of the Pacific volcanic arc with the South American Plate. As a result of this collision, a foreland developed west of the Sierra de Perijá and a forebulge appeared in the areas of Perijá and Lake Maracaibo. The forebulge became the raised Maracaibo basin, which restricted deposition and promoted erosion of the upper part of the K2 sequence (including the Aguardiente, Maraca, and lower Capacho sucessions, Fig. 2C) during the early Cenomanian. Therefore, the early Cenomanian beds of the La Grita Member were likely impacted by submarine erosion and/or non-deposition, thereby erasing the sedimentary record of this interval. Subsequently, renewed transgression rapidly flooded the area as a result of renewed compression and regional flexural downwarping in the Maracaibo basin (Canache et al., 1994).

5.2 Effect of diagenesis on stable isotope signatures

The usefulness of the isotope record of carbon and oxygen as paleoenvironmental proxies depends on the degree of post-depositional diagenetic alteration undergone by rocks (Algeo et al., 1992; Marshall, 1992). Indeed, the original stable isotope values

449 of carbonate sediment are susceptible to open-system diagenesis because of influxing
450 meteoric or burial fluids and the cementation of primary porosity (Immenhauser et al.,
451 2001; Moore, 2001; Phelps et al., 2015). Oxygen isotope values are more susceptible
452 to diagenetic alteration than carbon isotopes during burial diagenesis since oxygen
453 isotopes display significant fractioning with variations in temperature (Anderson and
454 Arthur, 1983; Marshall, 1992).

455 The $\delta^{13}C_{carb}$-$\delta^{18}O_{carb}$ crossplots have been succesfully used to assess the degree of
456 diagenetic alteration of the carbonate samples (e.g., Anderson and Arthur, 1983;
457 Marshal, 1992; Schobben et al., 2016). Figure 9 show that most of the samples have
458 late diagenetic alteration (Schobben et al., 2016). Late diagenesis occurs over the
459 period of deposition, when sediments are only lightly compacted, corresponding to
460 burial processes that act at depth over long geological periods (Flügel, 2004). This
461 diagram illustrates how the burial process acts as a closed system in which variations
462 only occur on the $\delta^{18}O_{carb}$ axis, since this variable is the most sensitive to the
463 temperature changes that occur with burial. So the cement precipitated during burial
464 (enriched in light isotopes) have greater influences on the change in oxygen isotope
465 values, whereas as the $\delta^{13}C_{carb}$ values remain practically constant (Marshall, 1992;
466 Bornemann et al., 2005). Therefore, we hypothesized that the observed $\delta^{18}O_{carb}$ pattern
467 (higher values in limestone beds and lower in marls; Fig. 6B) most likely reflects the
468 timing of burial diagenesis rather than changes in the palaeoceanic isotope signal
469 (such as salinity and temperature). Indeed, during burial diagenesis, limestone cement
470 forms early, at shallow depths and lower burial temperatures, and thus acquires higher
471 $\delta^{18}O$ values (~ -7 to 8‰) compared to marls (~ -11‰), which cement later (e.g.,
472 Algeo et al., 1992; Schrag et al., 1995; Rosales et al., 2004). In this context and

despite the diagenetic alteration of the $\delta^{18}O_{carb}$ signature, we can assume that the $\delta^{13}C_{carb}$ values probably represent a primary environmental signal.

5.3 The OAE-1d expression in the La Grita Member

Bréheret (1988) provided one of the first descriptions of OAE-1d in a geochemical study of episodes of organic-rich sedimentation from the Vocontian Basin (SE France), where the upper Albian contains a certain number of small beds (concentrated in a 10-meter-thick level) with a TOC% of 1–2%, termed the Breistroffer Level. Beds equivalent to OAE-1d have been described in detail from SE France (Breistroffer Level; Bréheret, 1988; Giraud et al., 2003; Bornemann et al., 2005), Romania (Melinte-Dobrinescu et al., 2015), Italy (Erbacher et al., 1996; Giorgioni et al., 2012; Gambacorta et al., 2015; 2016), Tunisia (Ben Fadhel et al., 2011), the United States (Robinson et al., 2008; Scott et al., 2013), and the Atlantic Ocean (Mazagan Plateau, Nederbragt et al., 2001; Leckie et al., 2002; Blake Nose Plateau, Wilson and Norris, 2001; Watkins et al., 2005; Fig. 1). This widespread distribution of carbon-enriched facies during the OAE-1d suggests a potentially global perturbation of the carbon cycle.

Based on biostratigraphy (*Rotalipora apenninica* Zone), carbon-isotope chemostratigraphic and higher TOC values, the OAE-1d positive CIE has been unambiguously identified in the La Grita Member (Fig. 6A). The increase in the TOC contents and the positive $\delta^{13}C_{carb}$ excursion are characteristic of different OAEs, including OAE-1d (Schlanger and Jenkyns, 1976; Jenkyns, 2010). The selective withdrawal of organic matter enriched in ^{12}C and its limited recycling causes the CO_2 in the ocean and atmospheric reservoirs to become enriched in ^{13}C during OAEs, leading a positive $\delta^{13}C$ excursion (Nemoto and Hasegawa, 2011). The positive $\delta^{13}C_{carb}$

498 anomaly observed at the onset of the OAE-1d in the La Grita Member is comparable
499 to the OAE-1d isotope expressions recorded in the Atlantic Ocean (Wilson and
500 Norris, 2001; Scott et al., 2013), in western Tethys (Bornemann et al., 2005; Gale et
501 al., 2011; Giorgioni et al., 2012), and in western Pacific Ocean (Navarro-Ramirez et
502 al., 2015; Fig. 10).

503 Pronounced $\delta^{13}C_{carb}$ cycles (~0.5 to 1%) observed in the calcareous shales,
504 limestone and shale from the La Grita Member (Fig. 6A-B) are the typical lithological
505 expression of the late Albian OAE-1d (Girogioni et al., 2012). The stratigraphic
506 distribution of $\delta^{13}C_{carb}$ in the *Rotalipora appenninica* Zone show a cyclical pattern
507 similar to those reported from the Umbria-Marche Basin (Figs. 6A,10). Giorgioni et
508 al. (2012) and Yao et al. (2018) suggest that the fluctuating monsoonal regime,
509 coupled with an unstable oceanic structure, made the oceanic carbon reservoir
510 sensitive to orbital variations during the mid-Cretaceous. However, a more detailed
511 cyclostratigraphic study is needed to elucidate these orbital cycles in the La Grita
512 Member.

513 Furthermore, the $\delta^{13}C_{org}$ values mostly lie between -28 and -26‰ throughout the
514 La Grita Member (Fig. 6C). These $\delta^{13}C_{org}$ values are typical of marine organic matter
515 accumulated during the mid-Cretaceous (Dean et al., 1986). Consequently, the change
516 in the $\delta^{13}C_{org}$ isotopic composition between the Aguardiente Formation and the La
517 Grita Member could correspond to a change in the source of the organic matter. Such
518 a change suggests a greater influence of terrestrial organic matter in the Aguardiente
519 Formation and a greater supply of marine organic matter in the La Grita Member as
520 transgression proceeded. Dean et al. (1986) attribute this difference to a greater
521 availability of dissolved CO_2 for marine algae because of the higher pCO_2 in the mid-
522 Cretaceous atmosphere.

523

524 **5.4 Paleoenvironmental conditions during the OAE-1d**

525 ***5.4.1 Continental weathering***

526 Changes in the weathering at the source areas and clastic influx that prevailed
527 during deposition of the La Grita Member are inferred using the siliciclastic balance,
528 Rb/Sr and Ti/Al ratios and CIA index (Li et al., 2003; Croudace and Rothwell, 2015;
529 Nesbitt and Young, 1982). Higher values in these detrital proxies could be interpreted
530 as: (1) heavier rainfall and enhanced continental weathering and runoff, and/or as (2)
531 lowered carbonate production in surface water. However, we must reject this last
532 hypothesis because the vertical distribution of Ca shows higher values (up to 60%)
533 during the OAE-1d relative to the rest of the succession. Therefore, in the La Grita
534 Member, the meaningful increase in the siliciclastic balance, Rb/Sr, Ti/Al ratios and
535 CIA index observed during the OAE-1d (*Rotalipora appenninica* Zone; Fig. 11A-D)
536 more likely suggests an enhanced continental weathering rates and detrital discharge
537 deriving from an accelerated hydrological cycle. Some authors (e.g., Wilson and
538 Norris, 2001; Leckie et al., 2002; Gambacorta et al., 2015; Navarro-Ramírez et al.,
539 2017) have concluded that the elevated pCO2 levels and greenhouse climate
540 prevailing during the OAE-1d induced an acceleration of the hydrologic cycle and an
541 increase in continental weathering rates. The elevated pCO2 levels were caused by the
542 release of CO_2 associated with the volcanic eruption of Hess Rise in the northern
543 Pacific Ocean (Eldholm and Coffin, 2000; Boudgher-Fadel, 2015) and/or to the
544 eruption of the central portion of the Kerguelen Plateau LIP (Richey et al., 2018; Fig.
545 1). These results are in good agreement with interpretations by Navarro-Ramírez et al.
546 (2017) that suggest also higher weathering rates in the Brazilian massif during the
547 mid-Cretaceous. Furthermore, the higher hydrolysing conditions recorded in the La

548 Grita Member may also favoured higher nutrient fluxes into the basins, ultimately
549 boosting primary productivity and the development of oxygen-depleted conditions
550 (Föllmi et al., 1994; Weissert et al., 1998; Jenkyns, 2010; Fantasia et al., 2018).

551 On the other hand, the vertical distribution of most of the detrital elements also
552 shows a cyclical variability (Fig. 7D). As discussed before, this variability may reflect
553 fluctuations in the rivers discharges possibly driven by longer-term (i.e., orbital) shifts
554 of the mean annual position of the Intertropical Convergence Zone (ITCZ), which
555 connects the large-scale precipitation and wind field patterns of the Hadley cells
556 (Borneman et al., 2005; Hofmann and Wagner, 2011; Giorgioni et al., 2012;
557 Hasegawa et al., 2012). Borneman et al. (2005) and Giorgioni et al. (2012) suggest
558 that long eccentricity cycles likely induced an exceptionally strong seasonal contrast,
559 at least in western Tethys, during the OAE-1d. These results support the idea that the
560 orbital forcing likely also modulated the equatorial monsoonal activity during the
561 OAE-1d (Borneman et al., 2005; Hofmann and Wagner, 2011; Giorgioni et al., 2012).

562 ***5.4.2 Redox conditions***

563 The redox conditions that prevailed during the deposition of the La Grita Member
564 are investigated using several proxies (Figs. 8 and 12): RSTE enrichment factors (U,
565 V, Mo, Cr, Ni, Zn), pyrite content, total sulfur, redox balance (V, Zn, U, Mo, Cr, Ni),
566 the ternary diagram TOC-S-Fe and U–Mo and Mo-TOC co-variation patterns.

567 Stratigraphic variations in the RSTE enrichment factors, pyrite content, total sulfur
568 and the redox balance show similar trends that suggest prevailing oxic conditions in
569 the Aguardiente and Maraca formations and anoxic-euxinic conditions in the La Grita
570 and Seboruco members (Fig. 8A-G). These results are in agreement with the TOC–S–
571 Fe relationship, which is commonly used to evaluate paleo-oxygenation conditions in
572 the sedimentary environment (Dean and Arthur, 1989; Rimmer et al., 2004; Montero-

573 Serrano et al., 2010b; Fig. 12A). The samples plot along a line of constant S/Fe ratio,
574 as in the present study (La Grita and Seboruco members), indicates anoxic deposition
575 conditions (similar conditions to the deposit of the La Luna Formation; Lo Mónaco et
576 al., 2002) and, the limiting factor in pyrite formation was not TOC content but the
577 quantity of detrital reactive Fe present (Raiswell and Berner, 1985; Arthur and
578 Sageman, 1994). However, at the boundary between the La Grita and Seboruco
579 members, the stratigraphic variations show that the anoxic conditions are interrupted
580 at 8.25 m by an abrupt change to dysoxic conditions. Based on the biostratigraphic
581 information discussed above, we hypothesize this change could be related to the
582 hiatus (Figs. 5 and 8H). After this episode, anoxic conditions were gradually re-
583 established, apparently due to a rapid basin subsidence (Canache et al., 1994).

584 Although the TOC content indicates prevailing anoxic conditions throughout the
585 entire depositional period of the La Grita Member, the RSTE only show two episodes
586 of strong enrichment (EF>10), at 3.50 m and at 8.25 m (Fig. 8A-B). This trend in the
587 RSTE can be interpreted as the cause of a basin reservoir effect (e.g., Algeo and
588 Lyons, 2006; Tribovillard et al., 2008; Algeo and Rowe, 2012) described for several
589 modern anoxic marine environments, in which a strong pycnocline or a restriction of
590 the basin induces dramatic isolation of the deep-water mass. In this environment, the
591 inventory of dissolved trace metals could become depleted as the sink flux of trace
592 metals to the sediments exceeds the input associated with deep-water renewal
593 (Tribovillard et al., 2008).

594 In addition, the patterns of U-Mo covariations coupled with trace-metal
595 concentrations versus TOC diagrams provide suitable information on the evolution of
596 paleoenvironmental marine systems, and in particular on water-mass restriction
597 (Algeo and Lyons, 2006; McArthur et al., 2008; Algeo and Tribovillard, 2009; Algeo

598 and Rowe, 2012; Tribovillard et al., 2012). This is due to the different geochemical
599 behaviour of U and Mo: (1) the uptake of authigenic U by marine sediments begins at
600 the Fe(II)–Fe(III) redox boundary (i.e., suboxic conditions), whereas authigenic Mo
601 enrichment requires the presence of H_2S (i.e., euxinic conditions), and (2) the transfer
602 of aqueous Mo to the sediment may be enhanced through particulate shuttles, whereas
603 aqueous U is unaffected by this process (Tribovillard et al., 2012).

604 The covariation in the EF of U-Mo for the corresponding samples of the La Grita
605 Member is illustrated in Figure 12B. The distribution of the samples exhibits greater
606 enrichment of Mo relative to U ($[Mo/U]_{agua\ de\ mar}$ 1-3 and >3), reflecting the operation
607 of a metal-oxyhydroxide particulate shuttle within the water column, over a range of
608 redox conditions, predominantly anoxic to probably euxinic (equal increases in Mo
609 and U; Algeo and Tribovillard, 2009; Tribovillard et al., 2012). This is typically the
610 feature observed in ancient and modern weakly restricted basins (e.g., La Luna
611 Formation in Maracaibo Basin and Cariaco Basin respectively; Algeo and
612 Tribovillard, 2009; Tribovillard et al., 2012). These interpretations are also in
613 agreement with the information given in the TOC vs. Mo diagram (Fig. 12C). Settings
614 in which deep waters were predominantly oxic or suboxic accumulate little authigenic
615 Mo because the concentrations of H_2S required to convert molybdate anions into
616 particle-reactive thiomolybdates are lacking (Helz et al., 1996). In such systems, the
617 low concentration of Mo is due to redox conditions rather than hydrographic controls.
618 However, in a restricted basin with low deep-water renewal, the inventory of
619 dissolved Mo is depleted and the Mo/TOC ratio is therefore low (Algeo and Rowe,
620 2012). Under this context, at the La Grita Member, reducing conditions are evident
621 and the medium Mo/TOC ratios suggest that this unit was deposited in a moderately
622 restricted marine system (Cariaco Basin-type; Fig. 12C).

5.4.3 Marine primary productivity: Inferences from phosphorus contents

P is an important limiting nutrient in the ocean, driving primary productivity (e.g., Tyrell, 1999; Schoepfer et al., 2015). The transfer of P into sediments occurs by its incorporation into OM and fish debris or by aggregation onto clay particles or iron and manganese oxyhydroxides (Delaney, 1998). However, P burial within sediments is strongly influenced by changes in the benthic redox conditions (e.g., van Cappellen and Ingall, 1994; Ingall et al., 2005; Algeo and Ingall, 2007; Mort et al., 2007; Schoepfer et al., 2015). Indeed, dysoxic-to-anoxic bottom-water conditions not only promote enhanced preservation of organic matter but also a remobilization and release of mineral-associated phosphate and organic P into the uppermost sediments and overlying water column (van Cappellen and Ingall, 1994; Ingall et al., 2005; Mort et al., 2007). Under such conditions, the increased regeneration of P in sediments may lead to both enhanced phosphate recycling (low P burial efficiency) and increased primary productivity in a positive feedback loop (van Cappellen and Ingall, 1994; Ingall et al., 2005; Schoepfer et al., 2015).

Two main processes have been proposed to explain the supply of P to marine basins and paleoproductivity increase: (1) reworking of nearshore sediments and soils during transgression (Erbacher et al., 1996; Jarvis et al., 2002) and (2) intensified precipitation and enhanced continental weathering and runoff (Föllmi, 1996). As shown in Figure 2a, the La Grita Member represents the period of maximum flooding in the third transgressive cycle proposed by Macellari (1988), with up to 80% of regional areas flooded (Macellari, 1988). Likewise, the detrital proxies (Fig. 11) evidence that the initial rise in P contents could be correlated with increased continental runoff and weathering. Overall, both processes probably contributed to an upswing in primary productivity, as suggested by the high TOC values (up to 8%).

However, the P contents in the La Grita Member show two spikes of heavy enrichment, at 3.50 m and 8.25 m of stratigraphic depth (similar to the RSTE trend, Figs.7c and 8E). This assumes that redox conditions dominated P behaviour above a detrital effect during deposition of the La Grita Member. Thus, we hypothesize that the transgression advance and the intensification of weathering gave rise to an initial rise in P concentrations and in primary productivity in the basin. During this first stage (Figs. 7C and 8E; 0–3 m), organic matter decay and PO_4^{3-} transfer likely led to an increase in the precipitation of $P_{authigenic}$ and $P_{oxyhydroxides\text{-}Fe}$ in deep water (Mort et al., 2007). Then, progressively more anoxic conditions and the conservation of organic matter inhibited the formation of $P_{authigenic}$, decreasing the concentration of P_{total} in the La Grita sediments. The recycling of phosphate and other nutrients from deep to surface water probably kept primary productivity high during and after OAE-1d.

Alternatively, P-rich intervals might also be related with a high abundance of preserved fish debris within the sediment (Schenau and De Lange, 2001; Montero-Serrano et al., 2015). Indeed, large amount of fish debris and P-rich autigenic phases have also been reported in previous petrographic analyses of the La Grita Member (Rodríguez, 1989).

5.5. Depositional model of the La Grita Member

The depositional system from the mid to late Cretaceous in western Venezuela was heavily influenced by the topographic landscape. The basin was characterized by emergent zones that acted as paleobathymetric barriers, giving rise to a series of semi-restricted basins with poor water circulation (Macellari, 1988; Lugo and Mann, 1995; Erlich et al., 1999a,b; Fig. 13A). Based on the geochemical data presented in this

673 study, we propose a depositional and environmental conditions model for the La Grita
674 Member (Fig. 13B). This model is detailed in the stages described below.
675 In the stage 1 the third transgressive cycle proposed by Macellari (1988) starts with
676 the deposition of the sandy sediments of the Aguardiente Formation in a littoral and/or
677 fluvial-coastal setting. This more proximal setting is characterized by oxic bottom
678 waters (low values of RSTE enrichment factors) and is influenced by terrestrial
679 organic matter evidenced by more positive $\delta^{13}C_{org}$ values (-26‰ to -23‰; Dean et al.,
680 1986; Meyers et al., 2006).
681 Subsequently, during stage 2 the acceleration of the hydrological cycle led to
682 increased runoff, as indicated by the meaningful increase in the detrital proxies (Fig.
683 11). This process probably generated an increase in nutrient availability and thus in
684 primary productivity. The enhanced runoff, together with basin deepening, led to a
685 thermohaline stratification and decrease in dissolved oxygen in the bottom water,
686 thereby favouring the preservation of organic matter. This rapid increase in primary
687 productivity created a rise in dissolved ^{13}C in ocean water since ^{12}C is preferentially
688 captured by organisms. The establishment of these anoxic bottom water conditions
689 caused strong RSTE enrichment in the La Grita sediments ($10 < EF < 1000$; Fig. 8A-
690 B) during the initial stages of the transgression.
691 In a more advanced stage of the transgression (stage 3), anoxic bottom water
692 conditions persisted, and the recycling of phosphate and other nutrients from deep
693 water probably kept primary productivity high. The semi-restriction of the basin due
694 to topographic highs and the increased water stratification (as illustrated by the Mo-U
695 and Mo-TOC co-variation patterns; Fig. 12B-C) probably prevented high metal
696 concentrations in the deep water (EF ~ 10; basin reservoir effect).

In the stage 4 the sequence is truncated due to uplift of the basin associated with the collision of the Pacific volcanic arc with the continental crust of South America (Canache et al., 1994), thereby producing a period of no deposition — a hiatus. This event was accompanied by partial oxygenation of deep water, as revealed in the decrease in the redox balance (Fig. 8G).

Reactivation of the basin's compression and regional flexural downwarping, leading to a rapid re-establishment of sea level (Canache et al., 1994; stage 5). This allowed anoxic conditions to reign and a strong enrichment of trace metals right after the hiatus. The detrital proxies suggest that deposition of the Seboruco Member was accompanied by deceleration of the hydrological cycle and, therefore, by decreased primary productivity.

6. Conclusions

In this study, we present a new multi-proxy record (including biostratigraphy, carbon-isotope, as well as major, minor, and trace metals) of the late Albian OAE-1d interval from the La Grita Member (Capacho Formation) in southwestern Venezuela. This multi-proxy record yields the following generalizations and conclusions:

(1) The biostratigraphic data assessed indicate that the La Grita sediments were deposited at 100–98 Ma (*Rotalipora appenninica* Zone; late Albian), the same age reported for OAE-1d. Furthermore, this analysis revealed a hiatus at the lower Cenomanian boundary that is probably related to the collision of the Pacific Arc with the South American Continental Plate.

(2) The positive $\delta^{13}C_{carb}$ excursion (~1‰) and higher TOC values recorded in the La Grita Member are associated with the development of the OAE-1d in western basin of Venezuela.

(3) The detrital proxies (notably, siliciclastic balance, Rb/Sr, Ti/Al and CIA index) support the idea that (a) the greenhouse climate prevailing during the OAE-1d led an acceleration of the hydrologic cycle and an increase in continental weathering rates, and (b) the orbital forcing likely also modulated the equatorial monsoonal activity during the late Albian.

(4) With the exception of the Aguardiente Formation, the redox-sensitive proxies [notably, redox balance, RSTE enrichment factors, pyrite content, and ternary plots TOC-S-Fe] indicate anoxic (and possibly euxinic) bottom-water conditions during deposition of the La Grita and Seboruco members. Under such conditions, the release of phosphorus from the sediments into the water column likely sustained the primary productivity, acting as a positive feedback loop.

(5) Mo-U and Mo-TOC co-variation patterns suggest a semi-restricted basin setting (similar to the Cariaco Basin) for the deposition of the La Grita sediments. Thus, the moderate accumulation of redox-sensitive trace metals recorded during the OAE-1d likely result from a basin reservoir effect.

Taken as a whole, our geochemical data complement scarce existing data from northern South America for Albian-Cenomanian records and provide a solid record of the major paleoenvironmental changes that fostered deposition of the La Grita Member during the development of the OAE-1d.

7. Acknowledgments

This research was financed by the *Consejo de Desarrollo Científico y Humanístico* (Universidad Central de Venezuela) through project 03.00.5661/07, the Natural Sciences and Engineering Research Council of Canada (NSERC) through Discovery

747 Grants to J.-C. Montero-Serrano, and by Global Affairs Canada. We also
748 acknowledge the financial support of the Canada Economic Development for Quebec
749 Regions (CED) for the acquisition of the X-ray fluorescence (Epsilon 3-XL). The
750 authors are also grateful to the Stable Isotopes laboratory of PDVSA-INTEVEP for
751 the isotopic analyses and to Olga Rey (UCV) for her help in the biostratigraphic
752 interpretation. We thank Christine Laurin for reviewing the grammar. Lastly, we
753 specially thank the editor Thomas Algeo and the two anonymous reviewers for their
754 constructive comments which helped improving the manuscript.

8. References

Alberdi-Genolet, M., Tocco, R., 1999. Trace metals and organic geochemistry of the Machiques Member (Aptian–Albian) and La Luna Formation (Cenomanian–Campanian), Venezuela. Chemical Geology 160, 19-38.

Algeo, T.J., Ingall, E., 2007. Sedimentary Corg:P ratios, paleocean ventilation, and Phanerozoic atmospheric pO_2. Palaeogeography, Palaeoclimatology, Palaeoecology 256,130-155.

Algeo, T.J., Lyons, T.W., 2006. Mo-total organic carbon covariation in modern anoxic marine environments: implications for analysis of paleoredox and paleohidrographic conditions. Paleoceanography 21, PA1016 23 pp.

Algeo, T.J., Maynard, J.B., 2004. Trace-element behavior and redox facies in core shales of Upper Pennsylvanian Kansas-Type cyclothems. Chemical Geology 206, 289-318.

Algeo, T.J., Rowe, H., 2012. Paleoceanographic applications of trace metal concentration data. Chemical Geology 324-325, 6-18.

Algeo, T.J., Tribovillard, N., 2009. Environmental analysis of paleoceanographic system based on molybdenum-uranium covariation. Chemical Geology 268, 211-225.

Algeo, T.J.,Wilkinson, B.H., Lohmann, K.C., 1992. Meteoric-burial diagenesis of Pennsylvanian carbonate: water/rock interactions and basin geothermics. Journal Sedimentary Petrology 62, 652–670.

Anderson, T.F., Arthur, M.A., 1983. Stable isotopes of oxygen and carbon and their application to sedimentologic and paleoenvironmental problems, in Arthur, M.A., Schlanger S.O., Jenkyns, H.C. 1987. The Cenomanian-Turonian Oceanic Event, II. Paleoceanographic controls on organic-matter production and preservation. In:

780 Brooks, J., Fleet, A. (Eds.), Marine Petroleum Source Rocks. Geological Society
781 Special Publication. 26, pp 401-420.
782 Arthur, M.A., Dean, W.E., Schlanger, S.O., 1985. Variations in the global carbon
783 cycle during the Cretaceous related to climate, volcanism and changes in
784 atmospheric CO2. In: Sundquist, E.T., Broecker, W.S. (Eds.), The Carbon Cycle and
785 Atmospheric CO2: Natural Variations Archean to Present. AGU Geophysical
786 Monograph, 32, pp. 504-529.
787 Arthur, M.A., Sageman, B.B., 1994. Marine black shales: a review of depositional
788 mechanisms and significance of ancient deposits. Annual Review of Earth and
789 Planetary Sciences 22, 499–551.
790 Arthur, M.A., Schlanger S.O., and Jenkyns, H.C. 1987. The Cenomanian-Turonian
791 Oceanic Event, II. Paleoceanographic controls on organic-matter production and
792 preservation. Marine Petroleum Source Rocks 26, 401-420.
793 Barron, E.J., Washington, W.M., 1985. Warm Cretaceous climates: high atmospheric
794 CO2 as a plausible mechanism. In: Sunquist, E.T., Broecker, W.S. (Eds.), The
795 Carbon Cycle and Atmospheric CO2: Natural Variations from Archean to Present.
796 AGU Geophysical Monograph 32, 546-553.
797 Baquero, M., Méndez Baamonde, J., Méndez, J., 2008. Extensión regional de los
798 eventos oceánicos anóxicos 1a y 1b en la cuenca de Maracaibo, Venezuela. XI
799 congreso latinoamericano de geoquímica orgánica. Isla de Margarita, Nueva Esparta,
800 Venezuela. p. 10-12
801 Ben Fadhel, M., Layeb, M., Hedfi, A., Ben Youssef, M., 2011. Albian oceanic anoxic
802 events in northen Tunisia: Biostratigraphic and geochemical insights. Cretaceous
803 Research 31, 685–699.

804 Bodin, S., Meissner, P., Janssen, N.M.M., Steuber, T., Mutterlose, J., 2015. Large
805 igneous provinces and organic carbon burial: controls on global temperature and
806 continental weathering during the Early Cretaceous. Global and Planetary Change
807 133, 238-253.
808 Bornemann, A., Pross, J., Reichelt, K., Herrle, J.O., Hemleben, C., Mutterlose, J.,
809 2005. Reconstruction of short-term palaeoceanographic changes during the
810 formation of the 'Niveau Breistroffer' (OAE 1d, SE France). Journal of the
811 Geological Society 162, 623-639.
812 BouDagher-Fadel, M.K., 2015. Biostratigraphic and geological significance of
813 planktonic foraminifera. UCL Press, University College, London. 312pp.
814 Bréhéret, J., 1988. Épisodies de sedimentation riche en matière organique dans les
815 marnes bleues d`age aptien et albien de la partie pélagique du bassin vocontian.
816 Bulletin de la Société Géologique de France 4, 349-356.
817 Brumsack, H.J., 2006. The trace metal content of recent organic carbon-rich
818 sediments: Implications for Cretaceous black shale formation. Palaeogeography,
819 Palaeoclimatology, Palaeoecology 232, 344-361.
820 Calvert, S.E., Pedersen, T.F., 2007. Chapter Fourteen Elemental Proxies for
821 Palaeoclimatic and Palaeoceanographic Variability in Marine Sediments:
822 Interpretation and Application. Developments in Marine Geology 1, 567-644.
823 Canache, M.; Pilloud, A.; Truskowsky, I.; Crux, J., and Gamarra, S., 1994. Revisión
824 estratigráfica de la sección cretácica del río Maraca, Serranía de Perijá, Venezuela.
825 V Simposio Bolivariano, Exploración Petrolera de las Cuencas Subandinas.
826 Sociedad Venezolana de Geólogos. Caracas, Memoria: 240-241.

827 Croudace, I., Rothwell, R., 2015. Micro-XRF studies of sediment cores: Applications
828 of a non-destructive tool for environmental sciences. Dordrecht, NL. Springer,
829 668 pp.
830 De Cabrera, S.; Sliter, W. and Jarvis, I., 1999. Integrated foraminiferal biostratigraphy
831 and chemostratigraphy of the Querecual Formation (Cretaceous), Eastern
832 Venezuela. The Journal of Foraminiferal Research 29, 487-499.
833 Dean, W.E., Arthur, M.A., 1989. Iron–sulfur–carbon relationships in organic-carbon-
834 rich sequences: Cretaceous Western Interior Seaway. American Journal of Science
835 289, 708–743.
836 Dean, W.E., Arthur, M.A., Claypool, G.E., 1986. Depletion of ^{13}C in Cretaceous
837 marine organic matter: Source, diagenetic, or environmental signal? Marine Geology
838 70, 119-157.
839 Delaney, M., 1998. Phosphorus accumulation in marine sediments and the oceanic
840 phosphorus cycle. Global Biogeochemical Cycles 12, 563-572.
841 Dunham, R.J., 1962. Classification of carbonate rocks according to depositional
842 texture, in Ham, W.E. (ed.), Classification of carbonate rocks: American
843 Association of Petroleum Geologists Memoir 108-121.
844 Egozcue, J.J., Pawlosky-Glahn, V., 2005. Group of parts and their balances in
845 compositional data analysis. Mathematical Geology 37, 795-828.
846 Eldholm, O., Coffin, M.F., 2000. Large igneous provinces and plate tectonics. In:
847 Richards, M.A., Gordon, R.G., van der Hilst, R.D. (Eds.), The History and
848 Dynamics of Global Plate Motions. American Geophysical Union Geophysical
849 Monograph 121, American Geophysical Union, Washington, DC, pp. 309–326.
850 Erba, E., 1994. Nannofossils and superplumes: The Early Aptian “nannoconid crisis”.
851 Paleoceanography 9, 483-501.

852 Erbacher, J., Hemleben, C., Huber, B.T., Markey, M., 1999. Correlating
853 environmental changes during early Albian oceanic anoxic event 1b using benthic
854 foraminiferal paleoecology. Marine Micropaleontology 38, 7-28.
855 Erbacher, J., Thurow, J., Littke, R., 1996. Evolution patterns of radiolaria and organic
856 matter variations: A new approach to identify sea level changes in mid-Cretaceous
857 pelagic environments. Geology 24, 499-502.
858 Erlich, R., Macsotay, O., Nederbragt, A., and Lorente, M.A. 1999a. Paleoecology,
859 Palaeoceanography and depositional environments of Upper Cretaceous rocks of
860 western Venezuela. Palaeogeography, Palaeoclimatology, Palaeoecology 153, 203-
861 238.
862 Erlich, R., Palmer-Koleman, S., and Lorente, M.A. 1999b. Geochemical
863 characterization of oceanographic and climatic changes recorded in Upper Albian
864 to Lower Maastrichtian strata, western Venezuela. Cretaceous Research 20, 547-
865 581.
866 Fantasia, A., Föllmi, K.B., Adatte, T., Spangenberg, J.E., Montero-Serrano, J.C.,
867 2018. The Early Toarcian oceanic anoxic event: Paleoenvironmnetal and
868 paleoclimatic change across the Alpine Tethys (Switzerland). Global and Planetary
869 Change 162, 53-68.
870 Fedo, C., Nesbitt, H.W., Young, G.M., 1995. Unravelling the effects of potassium
871 metasomatismin sedimentary rocks and paleosols, with implications for
872 paleoweathering conditions and provenance. Geology 23, 921–924.
873 Flügel, E., 2004, Microfacies of Carbonate Rocks, Analysis, Interpretation and
874 Application: Springer Verlag, Berlin, 976 pp.
875 Föllmi, K.B., 1996. The phosphorus cycle, phosphogenesis and marine phosphate-rich
876 deposits. Earth Science Reviews 40, 55–124.

877 Föllmi, K.B., Weissert, H., Bisping, M., Funk, H., 1994. Phosphogenesis, carbon
878 isotope stratigraphy, and carbonate-platform evolution along the Lower Cretaceous
879 northern Tethyan margin. Geological Society of America Bulletin 106, 729-746.
880 Gale, A., Jenkyns, H., Kennedy, W., Corfield, R., 1993. Chemostratigraphy versus
881 biostratigraphy: data from around the Cenomanian-Turonian boundary. Journal of
882 the Geological Society London 150, 29-32.
883 Gale, A.S., Bown, P., Caron, M., Crampton, J., Crowhurst, S.J., Kennedy, W.J.,
884 Petrizzo, M.R., Wray, D.S., 2011. The uppermost Middle and Upper Albian
885 succession at the Col de Palluel, Hautes-Alpes, France: An integrated study
886 (ammonites, inoceramid bivalves, planktonic foraminifera, nannofossils,
887 geochemistry, stable oxygen and carbon isotopes, cyclostratigraphy). Cretaceous
888 Research 32, 59-130.
889 Gambacorta, G., 2011. Paleoceanographic and paleoclimatic reconstruction of the
890 Albian-Cenomanian interval: from an unstable to a stable ocean. Università Degli
891 Studi di Milano. Scuola di dottorato Terra, Ambiente e Biodiversità. End year
892 progress report. 6 pp.
893 Gambacorta, G., Jenkyns, H.C., Russo, F., Tsikos, H., Wilson, P.A., Faucher, G.,
894 Erba. E., 2015. Carbon and oxygen isotope records of mid-Cretaceous Tethyan
895 pelagic sequences from the Umbria-Marche and Belluno Basins (Italy). Newsletters
896 on Stratigraphy 48, 299-323.
897 Gambacorta, G., Malinverno, A., Erba, E., 2016. Astronomical forcing on 'mid-
898 Cretaceous' C isotopic record in the Western Tethys. Geophysical Research
899 Abstracts. 18, EGU2016-12955-1.
900 Giorgioni, M., Weissert, H., Bernasconi S.M., Hochuli, P.A., Coccioni, R., Keller,
901 C.E. 2012. Orbital control on carbon cycle and oceanography in the mid

902 Cretaceous greenhouse, Paleoceanography 27, PA1204.
903 doi:10.1029/2011PA002163.
904 Giorgioni, M., Weissert, H., Bernsconi, S.M., Hochuli, P.A., Keller, C.E., Coccioni,
905 R., Petrizzo, M.R., Lukeneder, A., Garcia, T.I. 2015. Paleoceanographic changes
906 during the Albian-Cenomanian in the Tethys and Nort Atlantic and the onset of the
907 Cretaceous chalk. Global and Planetary Change 126, 46-61.
908 Giraud, F., Olivero, D., Baudin, F., Reboulet, S., Pittet, B., Proux, O., 2003. Minor
909 changes in surface-water fertility across the oceanic anoxic event 1d (late-Albian,
910 SE France) evidenced by calcareous nannofossils. International Journal of Earth
911 Sciences 92, 267-284.
912 González de Juana, C., Iturralde, J., and Picard, X., 1980. Geología de Venezuela y
913 sus cuencas petrolíferas. Ediciones Foninves, Caracas. 1031 pp.
914 Grunsky, E.C., Drew, L.J., Woodruff, L.G., Friske, P.W.B., Sutphin, D.M., 2013.
915 Statistical variability of the geochemistry and mineralogy of soils in the Maritime
916 Provinces of Canada and part of the Northeast United States. Geochemistry:
917 Exploration, Environment, Analysis 13(4), 249-266.
918 Helz G.R., Miller C.V., Charnock J.M., Mosselmans J.F.W., Pattrick R.A.D., Garner
919 C.D., Vaughan D.J., 1996. Mechanism of molybdenum removal from the sea and
920 its concentration in black shales: EXAFS evidence. Geochimica Cosmochimica
921 Acta 60, 3631–3642.
922 Herrle, J.O., Kössler, P., Friedrich, O., Erlenkeuser, H., Hemleben, C., 2004. High-
923 resolution carbon isotope records of the Aptian to Lower Albian from SE France and
924 the Mazagan Plateau (DSDP Site 545): A stratigraphic tool for paleoceanographic
925 and paleobiologic reconstruction. Earth and Planetary Science Letters 218, 149-161.

926 Hoffman, D.L., Algeo, T.J., Maynard, J.B., Joachimski, M.M., Hower, J.C., Jaminski,
927 J., 1998. Regional and stratigraphic variation in bottomwater anoxia in offshore
928 core shales of Upper Pennsylvanian cyclothems from the Eastern Midcontinent
929 Shelf (Kansas), USA. In: Schieber, J., Zimmerle, W., Sethi, P.S. (Eds.), Shales and
930 mudstones. vol. 1. Schweizerbart'sche, Stuttgart, 243–269.
931 Hofmann, P., Wagner, T., 2011. ITCZ controls on the Late Cretaceous black shale
932 sedimentation in the tropical Atlantic Ocean. Paleoceanography 26, PA4223.
933 Huber, B., Norris, R., MacLeod, K., 2002. Deep-sea paleotemperature record of
934 extreme warmth during Cretaceous. Geology 30, 123-126.
935 Immenhauser, A., van der Kooij, B., van Vliet, A., Schlager, W., Scott, R.W., 2001.
936 An ocean-facing Aptian-Albian carbonate margin, Oman. Sedimentology 48, 1187-
937 1207.
938 Ingall, E., Kolowith, L., Lyons, T., Hurtgen, M., 2005. Sediment carbon, nitrogen and
939 phosphorus cycling in an anoxic fjord, Effingham Inlet, British Columbia. American
940 Journal of Science 305, 240–258.
941 Jackson, S.E., 2008. Lamtrace data reduction software for LA-ICP-MS. In: Sylverster,
942 P. (Ed.), Laser Ablation ICP-MS in the Earth Sciences: Current Practices and
943 Outstanding Issues, volume 40 of Short Course Series. Mineralogical Association of
944 Canada, pp. 305-307.
945 Jackson. SE. 2001. The Application of Nd:YAG Lasers in LA-ICPMS. in Laser-
946 Ablation-ICPMS in the Earth Sciences: Principles and Applications. Laser-Ablation-
947 ICPMS in the Earth Sciences: Principles and Applications. Mineralogical
948 Association of Canada. St John's. pp. 29-45.
949 Jaminski, J., Algeo, T.J., Maynard, J.B., Hower, J.C., 1998. Climatic origin of dm-
950 scale compositional cyclicity in the Cleveland Member of the Ohio Shale (Upper

951 Devonian), Central Appalachian Basin, USA. In: Schieber, J., Zimmerle, W., Sethi,
952 P.S. (Eds.), Shales and mudstones. vol. 1. Schweizerbart'sche, Stuttgart, 217–242.
953 Jarvis, I., Mabrouk, A., Moody, R., de Cabrera, S., 2002. Late Cretaceous
954 (Campanian) carbon isotope events, sea-level change and correlation of the Tethyan
955 and Boreal realms. Palaeogeography, Palaeoclimatology, Palaeoecology 188, 215-
956 248.
957 Jenkyns, H. 1980. Cretaceous anoxic events: from continents to oceans. Journal of the
958 Geological Society 137, 171-188.
959 Jenkyns, H.C., 2010. Geochemistry of oceanic anoxic events. Geochemistry
960 Geophysics Geosystems 11, Q03004, doi:10.1029/2009GC002788.
961 Jones, B., Manning, D.A.C., 1994. Comparison of geochemical indices used for the
962 interpretation of palaeoredox conditions in ancient mudstones. Chemical Geology
963 111, 111–129.
964 Leckie, M., Bralower, T., and Cashman R., 2002. Oceanic anoxic events and plankton
965 evolution: Biotic response to tectonic forcing during the mid-Cretaceous.
966 Paleoceanography 17, 1-29.
967 Leite, T.D.F., Escalfoni, R., Da Fonseca. T.C.O., Miekeley, N., 2011. Determination
968 of major. minor and trace elements in rock samples by laser ablation inductively
969 coupled plasma mass spectrometry: Progress in the utilization of borate glasses as
970 targets. Spectrochimica Acta - Part B Atomic Spectroscopy 66, 314-320.
971 Li, X., Wei, G., Shao, L., Liu, Y., Liang, X., Jian, Z., Sun, M.,Wang, P., 2003.
972 Geochemical and Nd isotopic variations in sediments of the South China Sea: a
973 response to Cenozoic tectonism in SE Asia. Earth and Planetary Science Letters 211,
974 207-220.

975 Lo Mónaco, S., López, L., Rojas, H., Garcia, D., Premovic, P., Briceño, H., 2002.
976 Distribution of major and trace elements in the La Luna Formation, Southwestern
977 Venezuelan Basin. Organic Geochemistry 33, 1593-1608.
978 Lugo, J., Mann, P., 1995. Jurassic-Eocene tectonic evolution of Maracaibo Basin.
979 American Association of Petroleum Geologists 62, 698-725.
980 Macellari, C., 1988. Cretaceous paleogeography and depositional cycles of western
981 South America. Journal of South America Earth Science 4, 373-418.
982 Machado, M.C., Chemale F., Kawashita, K., Rey, O., Moura, C.A.V., 2016. Isotope
983 studies of carbonate rocks of La Luna Formation (Venezuela) to constrain the
984 oceanic anoxic event 3 (OAE3). Journal of South American Earth Sciences 72, 38-
985 48.
986 McLennan, S.M., Hemming, S., McDaniel, D.K., & Hanson, G.N., 1993.
987 Geochemical approaches to sedimentation, provenance, and tectonics. Geological
988 Society of America, Special Papers, 284, 21-40. doi:10.1130/spe284-p21.
989 Marshall, J.D., 1992. Climatic and oceanographic isotopic signals from the carbonate
990 rock record and their preservation. Geological Magazine 129, 143–160.
991 McArthur, J.M., Algeo, T.J., van de Schootbrugge, B., Li, Q., Howarth, R.J., 2008.
992 Basinal restriction, black shales, Re-Os dating, and the Early Toarcian (Jurassic)
993 oceanic anoxic event. Paleoceanography. 23, PA4217.
994 Melinte-Dobrinescu, M., Roban, R.D., Stoica, M., 2015. Palaeoenvironmental
995 changes across the Albian-Cenomanian boundary interval of the Eastern
996 Carpathians. Cretaceous Research 54, 68–85.
997 Méndez, J., Molina, A., Lobo, C., Pautt, A., and Luzardo, F. 2015. Feasibility of La
998 Grita Member of Early Cretaceous as a possible unconventional reservoir play, case
999 study, Western Venezuela. Society of Petroleum Engineers. SPE-177099-MS.

1000 Méndez B.J., Baquero M., Méndez Dot J.A. 2008. Calizas pelágicas derivadas de
1001 eventos oceánicos anóxicos en la Formación Apón del Grupo Cogollo. Cuenca de
1002 Maracaibo. Venezuela. In: II ALAGO. Congreso Latinoamericano de Geoquímica
1003 Orgánica. Caracas. p. 6-18.
1004 Méndez-Dot, J.A., Méndez-Baamonde, J., Reyes, D., Whilchy, R., 2015. The Cogollo
1005 Group and the oceanic anoxic events 1a and 1b, Maracaibo, Venezuela. Brazilian
1006 Journal of Geology 45, 41-61.
1007 Menegatti, A.P., Weissert, H., Brown, R.S., Tyson, R.V., Farimond, P., Strasser, A.,
1008 Caron, M., 1998. High-resolution δ13C stratigraphytrhough the early Aptian
1009 "Livello Salli" of the Alpine Thethys. Paleoceanography 13, 530–545.
1010 Meyers, P., Bernasconi, S., Forster, A. 2006. Origins and accumulation of organic
1011 matter in expanded Albian to Santonian black shale sequences on the Demerara
1012 Rise, South American Margin. Organic Geochemistry 37, 1816–1830.
1013 Montero-Serrano, J.C., Föllmi, K.B., Adatte, T., Spangenberg, J.E., Tribovillard, N.,
1014 Fantasia, A., Suan, G., 2015. Continental weathering and redox conditions during
1015 the early Toarcian Oceanic Anoxic Avent in the northwestern Tethys: Insight from
1016 the Posidonia Shale section in the Swiss Jura Mountains. Palaeogeography,
1017 Palaeoclimatology, Palaeoecology 429, 83–99.
1018 Montero-Serrano, J.C., Palarea-Albaladejo,J., Martín-Fernández, J.A., Martínez-
1019 Santana, M., Gutiérrez-Martín, J.V., 2010a. Sedimentary chemofacies
1020 characterization by means of multivariate analysis. Sedimentary Geology 228, 218–
1021 228.
1022 Montero-Serrano, J.C., Martínez, M., Riboulleau, A., Tribovillard, N., Márquez, G.,
1023 Gutiérrez-Martín, J.V., 2010b. Assessment of the oil source-rock potential of the

1024 Pedregoso Formation (Early Miocene) in the Falcón Basin of northwestern
1025 Venezuela. Marine and Petroleum Geology, 27(5), 1107-1118.
1026 Moore, C.H., 2001. Carbonate reservoirs, porosity evolution and diagenesis in a
1027 sequence stratigraphic framework. Elsevier, New York, 444 pp.
1028 Mort, H., Adatte, T., Föllmi, K., Keller, G., Steinmann, P., Matera, V., Berner, Z.,
1029 Stüben, D., 2007. Phosphorus and the roles of productivity and nutrient recycling
1030 during oceanic anoxic event 2. Geology 35, 483-486.
1031 Navarro-Ramírez, J.P., Bodin, S., Consorti, L., Immenhauser, A., 2017. Response of
1032 western South American epeiric-neritic ecosystem to middle Cretaceous Oceanic
1033 Anoxic Events. Cretaceous Research 75, 61–80.
1034 Navarro-Ramirez, J.P., Bodin, S., Heimhofer, U., Immenhauser, A., 2015. Record of
1035 Albian to early Cenomanian environmental perturbation in the eastern subequatorial
1036 Pacific. Palaeogeography, Palaeoclimatology, Palaeoecology 423, 122–137.
1037 Nederbragt, A., Fiorentino, A., Klosowska, B., 2001. Quantitative analysis of
1038 calcareous microfossils across the Albian-Cenomanian boundary oceanic anoxic
1039 event at DSDP Site 547 (North Atlantic). Palaeogeography, Palaeoclimatology,
1040 Palaeoecology 166, 401–421.
1041 Nemoto, T., Hasegawa, T., 2011. Submillenial resolution carbon isotope stratigraphy
1042 across the Oceanic Anoxic Event 2 horizon in the Tappu section, Hokkaido, Japan.
1043 Palaeogeography, Palaeoclimatology, Palaeoecology 309, 271–280.
1044 Nesbitt, H.W., Young, G.M., 1982. Early Proterozoic climates and plate motions
1045 inferred from major element chemistry of lutites. Nature 299, 715–717.
1046 Parnaud, F., Gou, Y., Pascual, J.C., Capello, M.A., Truskowski, I., Passalacqua, H.,
1047 1995. Stratigraphic synthesis of Western Venezuela. In: Tankard, J., Suárez,

1048 R.,Welsink, H.J. (Eds.), Petroleum Basins of South America. AAPG Memoir 62,
1049 681–698.
1050 Pawlowsky-Glahn, V., Egozcue, J.J., 2011. Exploring Compositional Data with the
1051 CoDa-Dendrogram. Austrian Journal of Statistics 40, 103–113.
1052 Pérez-Infante, J., Farrimond, P., and Furrer, M., 1996. Global and local controls
1053 influencing the deposition of the La Luna Formation (Cenomanian-Campanian),
1054 Western Venezuela. Chemical Geology 130, 271–288.
1055 Phelps, R., Kerans, C., Da-Gama, R., Jeremiah, J., Hull, D., Loucks, R., 2015.
1056 Response and recovery of the Comanche carbonate platform surrounding multiple
1057 Cretaceous oceanic anoxic events, northern Gulf of Mexico. Cretaceous Research
1058 54, 117–144.
1059 Pindell, J. L., 1985, Alleghanian reconstruction and subsequent evolution of the Gulf
1060 of Mexico, Bahamas, and ProtoCaribbean. Tectonics 4, 1–39.
1061 Pindell, J. L., 1993, Regional synopsis of Gulf of Mexico and Caribbean evolution, in
1062 J. L. Pindell, and B. F. Perkins, eds., Mesozoic and Early Cenozoic Development of
1063 the Gulf of Mexico and Caribbean Region: A Context for Hydrocarbon
1064 Exploration. Selected Papers Presented at the G.C.S.S.E.P.M Foundation
1065 Thirteenth Annual Research Conference , 251–274.
1066 Premoli Silva, I., Sliter, W.V., 1995. Cretaceous planktonic foraminiferal
1067 biostratigraphy and evolutionary trends from the Bottaccione section, Gubbio, Italy.
1068 Paleontographia Italica 82, 1-89.
1069 Premoli Silva, I., Verga, D., 2004. Practical manual of Cretaceous planktonic
1070 foraminifera: Perugia, Tipografía Pontefelcino, 283 pp.
1071 Raiswell, R., Berner, R. A., 1985. Pyrite formation in euxinic and semi-euxinic
1072 sediments, American Journal of Science 285, 710-724.

1073 Reátegui, K., Martínez,M., Esteves, I., Gutiérrez, J.V., Martínez, A., Meléndez,W.,
1074 Urbani, F., 2005. Geochemistry of the Mirador Formation (Late Eocene–Early
1075 Oligocene), south western Venezuela: Chemostratigraphic constraints on
1076 provenance and the influence of the sea level. Geochemical Journal 39, 213–226.
1077 Reimann, C., Filzmoser, P., Garrett, R.G., Dutter, R., 2008. Statistical data analysis
1078 explained – Applied environmental statistics with R. John Wiley, Chichester, 362
1079 pp.
1080 Renz, O. 1959. Estratigrafía del Cretáceo en Venezuela occidental. Boletín Geológico.
1081 5, 3–58.
1082 Rey, O., Simo, J., and Lorente, M.A. 2004. A record of long- and short-term
1083 environmental and climatic change during OAE-3: La Luna Formation, Late
1084 Cretaceous (Santonian-early Campanian), Venezuela. Sedimentary Geology 170,
1085 85–105.
1086 Richey, J., Upchurcha., Montañez, I., Lomax, B., Suarez, M., Croutc, N., Joeckel, R,
1087 Ludvigson, G., Smith, J. 2018. Changes in CO_2 during Ocean Anoxic Event 1d
1088 indicate similarities to other carbon cycle perturbations. Earth and Planetary Science
1089 Letters 491, 172-182.
1090 Rimmer, S.M., Thompson, J.A., Goodnight, S.A., Robl, T.L., 2004. Multiple controls
1091 of the preservation of organic matter in Devonian-Mississippian marine black
1092 shales: geochemical and petrographic evidence. Palaeogeography,
1093 Palaeoclimatology, Palaeoecology 215, 125–154.
1094 Robinson, S. A., Clarke, L.J., Nederbragt, A., Wood, I.G., 2008. Mid-Cretaceous
1095 oceanic anoxic events in the Pacific revealed by carbon-isotope stratigraphy of the
1096 Calera Limestone, California, USA, Geological Society of America Bulletin. 120,
1097 1416-1427.

1098 Robinson, S.A., Williams, T., and Bown, P.R., 2004, Fluctuations in biosiliceous
1099 production and the generation of Early Cretaceous oceanic anoxic events in the
1100 Pacific Ocean (ODP Leg 198, Shatsky Rise): Paleoceanography. 19, doi:
1101 10.1029/2004PA001010.
1102 Rodríguez, J. 1989. Estudio Geológico de una zona ubicada al norte de las
1103 poblaciones Zea y Santa Cruz de Mora, Distrito Tovar, Estado Mérida. Universidad
1104 Central de Venezuela. Escuela de Ingeniería. 259 pp.
1105 Rosales, I., Quesada, S., Robles, S., 2004. Paleotemperature variations of Early
1106 Jurassic seawater recorded in geochemical trends of belemnites from the Basque-
1107 Cantabrian basin, northern Spain. Palaeogeography, Palaeoclimatology,
1108 Palaeoecology 203, 253–275.
1109 Schenau, S.J., de Lange, G.J., 2001. Phosphorus regeneration vs. burial in sediments
1110 of the Arabian Sea. Marine Chemistry 75, 201–207.
1111 Schlanger, S. O., Jenkyns, H. C. 1976. Cretaceous oceanic anoxic events: Causes and
1112 consequences. Geologie en Mijnbouw 55, 170–184.
1113 Schobben, M., Ullmann, C., Leda, L., Korn, D., Struck, U., Reimold, W., Ghaderi, A.,
1114 Algeo, T.J., Korte, C., 2016. Discerning primary versus diagenetic signals in
1115 carbonate carbon and oxygen isotope records: An example from the Permian-
1116 Triassic boundary of Iran. Chemical Geology 422, 94–107.
1117 Scholle, P.A., Arthur, M.A., 1980. Carbon isotope fluctuations in Cretaceous pelagic
1118 limestones — Potential stratigraphic and petroleum-exploration tool. The American
1119 Association of Petroleum Geologists Bulletin 64, 67–87.
1120 Schoepfer, S.D., Shen, J., Wei, H., Tyson, R.V., Ingall, E. and Algeo, T.J., 2015.
1121 Total organic carbon, organic phosphorus, and biogenic barium fluxes as proxies for
1122 paleomarine productivity. Earth-Science Reviews, 149, 23-52.

1123 Schrag, D.P., De Paolo, D.J., Richter, F.M., 1995. Reconstructing past sea surface
1124 temperaturas from oxygen isotope measurements of bulk carbonate. Geochimica et
1125 Cosmochimica Acta 59, 2265–2278.
1126 Scott, R.W., Formolo, M., Rush, N., Owens, J.D., Oboh-Ikuenobe, F., 2013. Upper
1127 Albian OAE 1d event in the Chihuahua Trough, New Mexico, U.S.A. Cretaceous
1128 Research 46, 136–150.
1129 Sliter W.V., 1989. Biostratigraphic zonation for Cretaceous planktonic foraminfers
1130 examined in thin section. Journal of Foraminiferal Research 19, 1–19.
1131 Talukdar, S., Marcano, F., 1994. Petroleum system of the Maracaibo Basin,
1132 Venezuela. AAPG Memory. 60, 463–481.
1133 Talukdar, S., Gallango, O., Ruggiero, A., 1985. Formaciones La Luna y Querecual en
1134 Venezuela: Rocas madres de petróleo. Memorias del VI Congreso Geológico
1135 Venezolano, Tomo VI, p. 3006–3642.
1136 Tribovillard, N., Algeo, T.J., Lyons, T.W., Riboulleau, A., 2006. Trace metals as
1137 paleoredox and paleoproductivity proxies: An update. Chemical Geology 232, 12–
1138 32.
1139 Tribovillard, N., Bout-Roumazeilles, V., Algeo, T., Lyons, T., Sionneau, T., Montero-
1140 Serrano, J., Riboulleau, A., Baudin, F., 2008. Paleodepositional conditions in the
1141 Orca Basin as inferred from organic matter and trace metal contents. Marine
1142 Geology 254, 62–72.
1143 Tribovillard, N., Sansjofre, P., Aderm, M., Trentesux, A., Averbuch, O., Barbecot, F.,
1144 2012. Early diagenetic carbonate bed formation at the sediment-water interface
1145 triggered by synsedimentary faults. Chemical Geology 300–301, 1–13.
1146 Tribovillard, N.P., Stephan, J.F., Manivit, H., Reyre, Y., Cotillon, P., Jautée, E., 1991.
1147 Cretaceous black shales of Venezuelan Andes: Preliminary results on stratigraphy

and paleoenvironmental interpretations. Palaeogeography, Palaeoclimatology, Palaeoecology 81, 313–321.

Truskowski I. 2006. Calibración bioestratigráfica y correlación con datos geoquímicos de la Formación Querecual en su localidad tipo. Trabajo de Grado de Especialización en Geoquímica de Hidrocarburos. Facultad de Ciencias, Universidad Central de Venezuela. 106 pp.

Turgeon, S., Brumsack, H.J., 2006. Anoxic vs. dysoxic events reflected in sediment geochemistry during the Cenomanian-Turonian Boundary Event (Cretaceous) in the Umbria-Marche basin of Italy. Chemical Geology 234, 321–339.

Tyrell, T., 1999. The relative influences of nitrogen and phosphorus on oceanic primary production. Nature 400, 525-531. doi:10.1038/22941

Van Cappellen, P., Ingall, E.D., 1994. Benthic phosphorus regeneration, net primary production, and ocean anoxia: A model of the coupled marine biogeochemical cycles of carbon and phosphorus. Paleoceanography 9, 677–692.

van den Boogaart, K.G., Tolosana-Delgado, R., 2008. "Compositions": A unified R package to analyze compositional data. Computers and Geosciences 34, 320–338.

Villamil, T., Arango,C., Hay, W., 1999. Plate tectonic paleoceanographic hypothesis for Cretaceous source rocks and cherts of northern South America. In: Barrera, E., Johnson, C.C. (Eds.), evolution of the Cretaceous Ocean-Climate System. Geological Society of America. Special Paper 332, 191–201.

Villamil, T., Pindell, J., 1998. Mesozoic paleogeographic evolution of northern South America: Foundations for sequence stratigraphic studies in passive margin strata deposited during nonglacial times. In: Pindell, J.L., Drake, Ch. (Eds.), Paleogeographic Evolution and Non-Glacial Eustasy, Northern South America. SEPM Special Publication. 58, 283–318.

1173 Vrielynck, B., Bouysse, P., 2003. The Changing Face of the Earth. Commission for
1174 the Geological Map of the World, CCGM-UNESCO Publishing. 32 p., 11 pl.
1175 Watkins, D., Cooper, M., Wilson, P. 2005. Calcareous nannoplankton response to late
1176 Albian oceanic anoxic event 1d in the Western North Atlantic. Paleoceanography
1177 20, 1–14.
1178 Wagreich, M., 2012. “OAE 3” e regional Atlantic organic carbon burial during the
1179 Coniacian-Santonian. Climate of the Past 8, 1447-1455.
1180 Wedepohl, K.H., 1991. The composition of the upper Earth's crust and the natural
1181 cycles of selected elements. Metals in natural raw materials. Natural resources. In:
1182 Merian, E. (Ed.), Metals and their compounds in the natural environment. VCH,
1183 Weinheim, Germany, 3–17.
1184 Wegner. C., Bennett. K.E., Vernal. A.D., Forwick, M., Fritz, M., Heikkilä, M., Łącka,
1185 M., Lantuit, H., Laska, M., Moskalik, M., O'Regan, M., Pawłowska, J., Promińska,
1186 A., Rachold, V., Vonk, J.E., Werner, K., 2015. Variability in transport of terrigenous
1187 material on the shelves and the deep Arctic Ocean during the Holocene. Polar
1188 Research 34, 1-19. DOI: 10.3402/polar.v34.24964.
1189 Weissert, H., Lini, A., Föllmi, K.B., Kuhn, O., 1998. Correlation of Early Cretaceous
1190 Carbon isotope stratigraphy and platform drowning events: a possible link?.
1191 Palaeogeography, Palaeoclimatology, Palaeoecology 137, 189-203.
1192 Wilson, P., Norris, R., 2001. Warm tropical ocean surface and global anoxia during
1193 mid-Cretaceous period. Nature 412, 425–428.
1194 Yao, H., Chen, X., Melinte-Dobrinescu, M., Wu, H., Liang, H., Weissert, H., 2018.
1195 Biostratigraphy,carbon isotopes and cyclostratigraphy of the Albian-Cenomanian
1196 transition and Oceanic Anoxic Event 1d in southern Tibet. Palaeogeography,
1197 Palaeoclimatology, Palaeoecology 499, 45-55

Young, R.A., 1993. The Rietveld Method. International Union of Crystallography Monographs on Crystallography 5. [Chester, England]: Oxford; New York: International Union of Crystallograhy; Oxford University Press, 308 p.

Appendix A. Supplementary material

Supplementary data associated with this article can be found in the online version at http…

Figure captions

Fig. 1. Palaeogeographical maps of the Albian-Cenomanian boundary (redrawn from Vrielynck and Bouysse, 2003) showing the La Grita Member studied herein and the locations of the well-dated DSP and ODP sites (black dots) that recorded the OAE-1d (Wilson and Norris, 2001).

Fig. 2. **(A)** General chart of stratigraphic correlation of the Cretaceous in western Venezuela (synthesized by Erlich et al., 1999b); **(B)** Location maps; **(C)** the different deposition cycles (Macellari, 1988), global sea level changes (Sliter, 1976), and the percentage of flooded areas in northern South America (Maceralli, 1988); **(D)** the proposed stratigraphic analysis for the La Grita Member (Méndez et al., 2015). The Sequence K2 refers to the depositional sequence Albian–lower Cenomanian described by Parnaud et al. (1995) and includes the Lisure, Maraca, lower Capacho, Aguardiente, and basal Escandalosa formations. TRS: Transgressive ravinement surface, MFS: Maximun flooding surface, HST: Highstand systems tract, TST: Transgressive systems tract.

Fig. 3. Stratigraphic column with the distribution of the samples studied herein and outcrop of the La Grita Member on the Guaruríes River (Zea, state of Mérida, Venezuela).

Fig. 4. Microphotographs of the planktonic foraminifer species identified in the study section: **(A)** *Rotalipora* cf *Ticinesis* (ZEARG-185), **(B)** *Hedbergella delrioensis* (ZEARG-185), **(C)** *Hedbergella rischi* (ZEARG-165), **(D)** *Hedbergella planispira* (ZEARG-85), **(E)** *Clavihedbergella simplex* (ZEARG-155), **(F)** *Ticinella raynaudi* (ZEARG-125), **(G)** *Ticinella roberti* (ZEARG-112), and **(H)** *Ticinella primula* ZEARG-155).

Fig. 4. Continuation: **(I)** *Whiteinella báltica* (ZEARG-65), **(J)** *Biticinella bregginesis* (ZEARG-145), **(K)** *Globigerinelloides caseyi* (ZEARG-95), **(L)** *Globigerinelloides ultramicrus* (ZEARG-115), **(M)** *Globigerinelloides bentonesis* (ZEARG-185), **(N)** *Planomalina buxtorfi* (ZEARG-112), **(O)** *Heterohelix morenami* (ZEARG-85), and **(P)** *Heterohelix reussi* (ZEARG-85). All the microphotographs were taken with parallel nichols.

Fig. 5. Distribution of the main species of marker and/or indicator planktonic foraminifera and biostratigraphic Zones identified in the La Grita Member. Note that the interval corresponding to the early Cenomanian (*Rotalipora brotzeni-Rotalipora reicheli* Zones) cannot be defined due to a lack of biostratigraphic data.

Fig. 6. Stratigraphic distribution of isotope compositions of **(A)** $\delta^{13}C_{carb}$, **(B)** $\delta^{18}O_{carb,}$ **(C)** $\delta^{13}C_{org}$, **(D)** total organic carbon (TOC), and **(E)** relative sea level in the La Grita

1249 section. The shaded interval indicates the positive carbon isotope excursion
1250 (*Rotalipora appenninica* Zone) related to OAE-1d.
1251
1252 **Fig. 7**. **(A-E)** Stratigraphic profiles of the major geochemical associations obtained by
1253 compositional Q-mode cluster analysis. The shaded interval indicates the positive
1254 carbon isotope excursion (*Rotalipora appenninica* Zone) related to OAE-1d. **(F)**
1255 Dendrogram of association of variables obtained by applying Ward clustering
1256 algorithm based on the variation matrix of elemental geochemical dataset.
1257
1258 **Fig. 8**. Stratigraphic distribution of the main redox proxies obtained from the La Grita
1259 Member. **(A-B)** Element enrichment factors (EF) for the redox associations; **(C)**
1260 relative content of pyrite (%); **(D)** sulfur total (%); **(E)** P enrichment factors; **(G)**
1261 redox balances; Balances are represented according to Eq. (1); **(H)** relative sea level
1262 in the La Grita section. The shaded interval indicates the positive carbon isotope
1263 excursion (*Rotalipora appenninica* Zone) related to OAE-1d.
1264
1265 **Fig. 9**. $\delta^{13}C_{carb}$ vs. $\delta^{18}O_{carb}$ correlation diagram for the various units studied, indicating
1266 zones altered by different diagenic processes (according to Schobben et al., 2016).
1267
1268 **Fig. 10**. Overview of Albian/Cenomanian carbon-isotope records showing OAE-1d
1269 (shaded interval) in different basins worldwide.
1270
1271 **Fig. 11**. Stratigraphic distribution of the main detrital proxies obtained from the La
1272 Grita Member. **(A)** detrital balance (Sc, K, Al, Rb, Si, Zr, Hf, Ti, Nb). Balances are
1273 represented according to Eq. (1). **(B)**. Rb/Sr; **(C)** Ti/Al; (D) CIA index. The shaded

1274 interval indicates the positive carbon isotope excursion (*Rotalipora appenninica*
1275 Zone) related to OAE-1d.
1276
1277 **Fig. 12**. **(A)** TOC–S–Fe ternary diagram corresponding to the La Grita Member used
1278 to discriminate between different redox facies (La Luna data are from Lo Mónaco et
1279 al., 2002). **(B)** U-Mo covariation for evaluating redox and oceanographic controls in
1280 the La Grita Member, based on the model proposed by Tribovillard et al. (2009). **(C)**
1281 Mo-TOC covariation for the La Grita samples, indicating some trends for modern
1282 restricted and semi-restricted basins (modified after Algeo and Rowe, 2012).
1283
1284 **Fig. 13**. Depositional model of the La Grita Member: **(A)** Physiography and a-a'
1285 cross-section of basin, and **(B)** model to illustrate the various stages and geochemical
1286 processes characteristic during the development of the OAE-1d. OMZ: oxygen
1287 minimum zone.

Figure 1

(Simgle column)

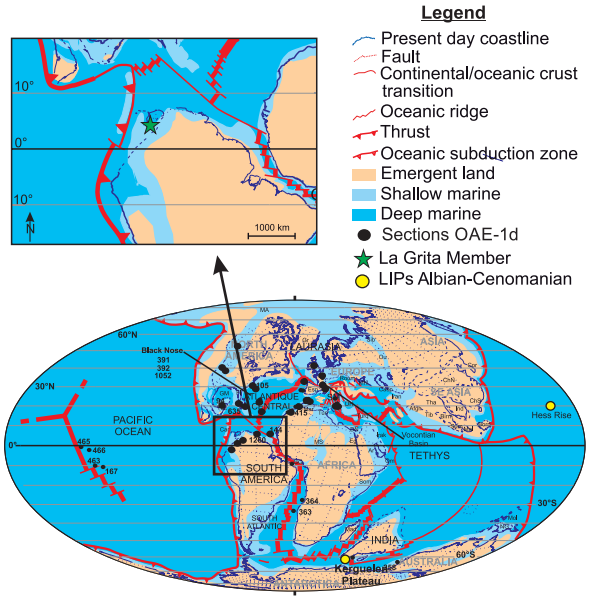

Albian-Cenomanian (~100 Ma)

Figure 2

(Double column-full page width)

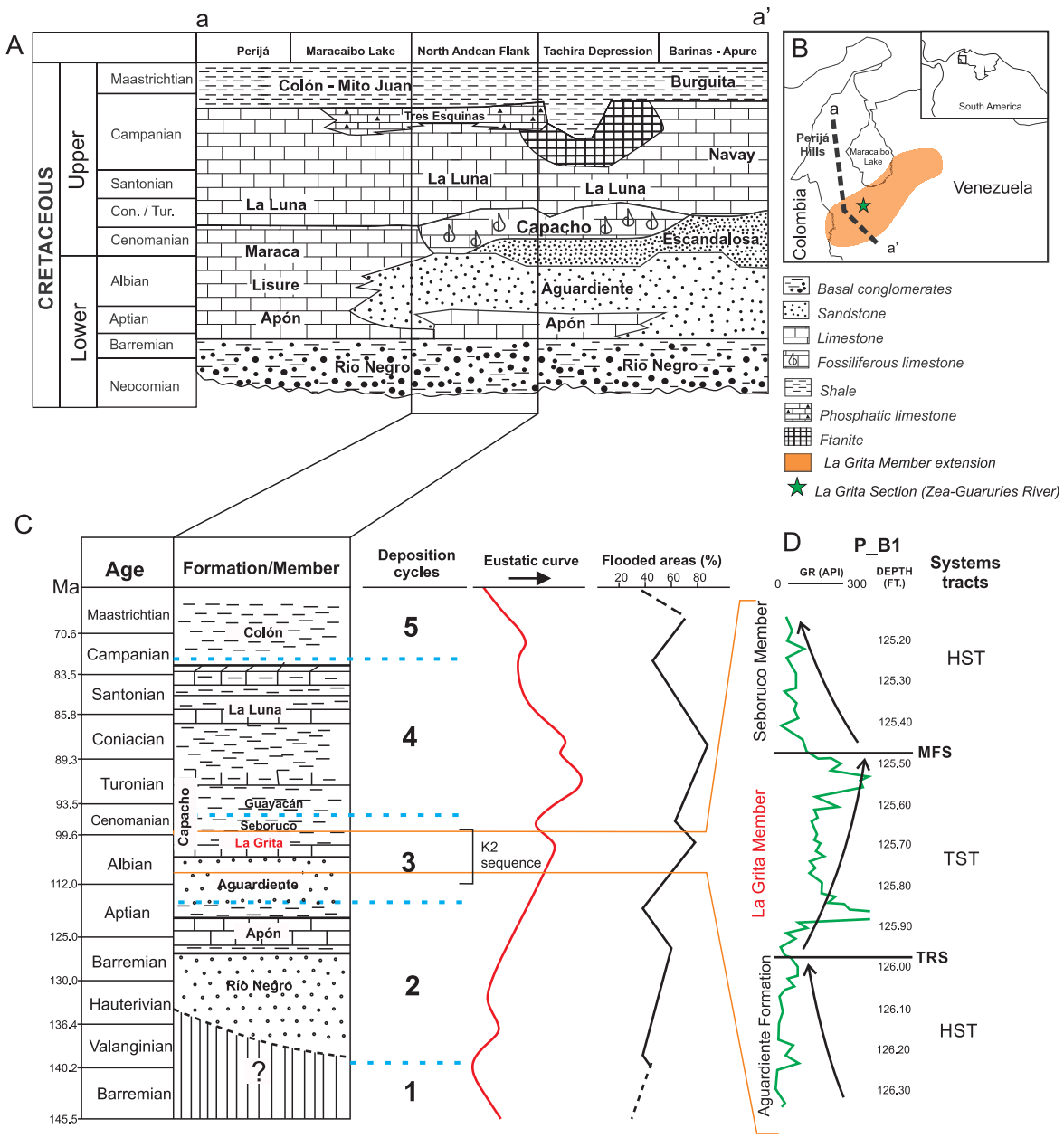

Figure 3

(Double column-full page width)

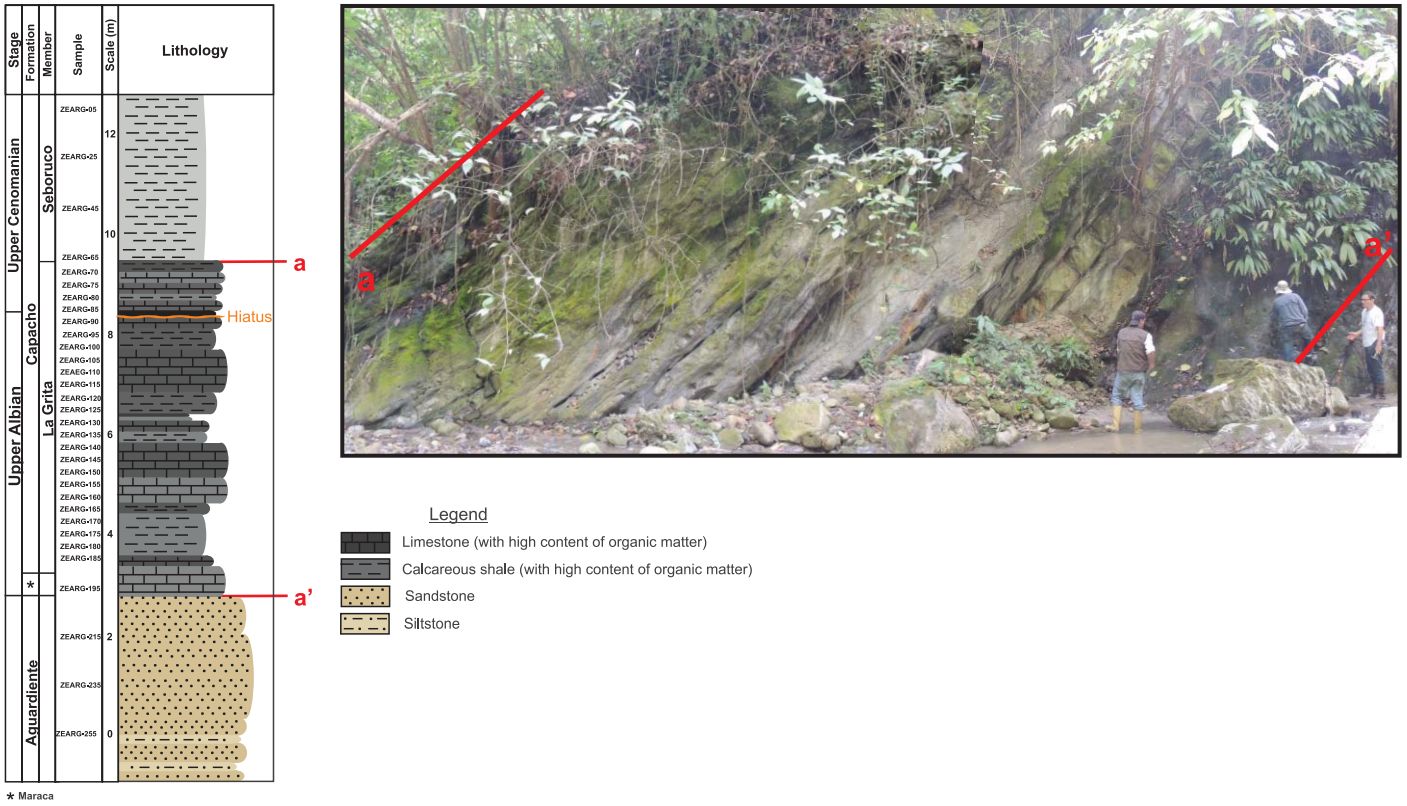

Figure 4

(Double column-full page width)

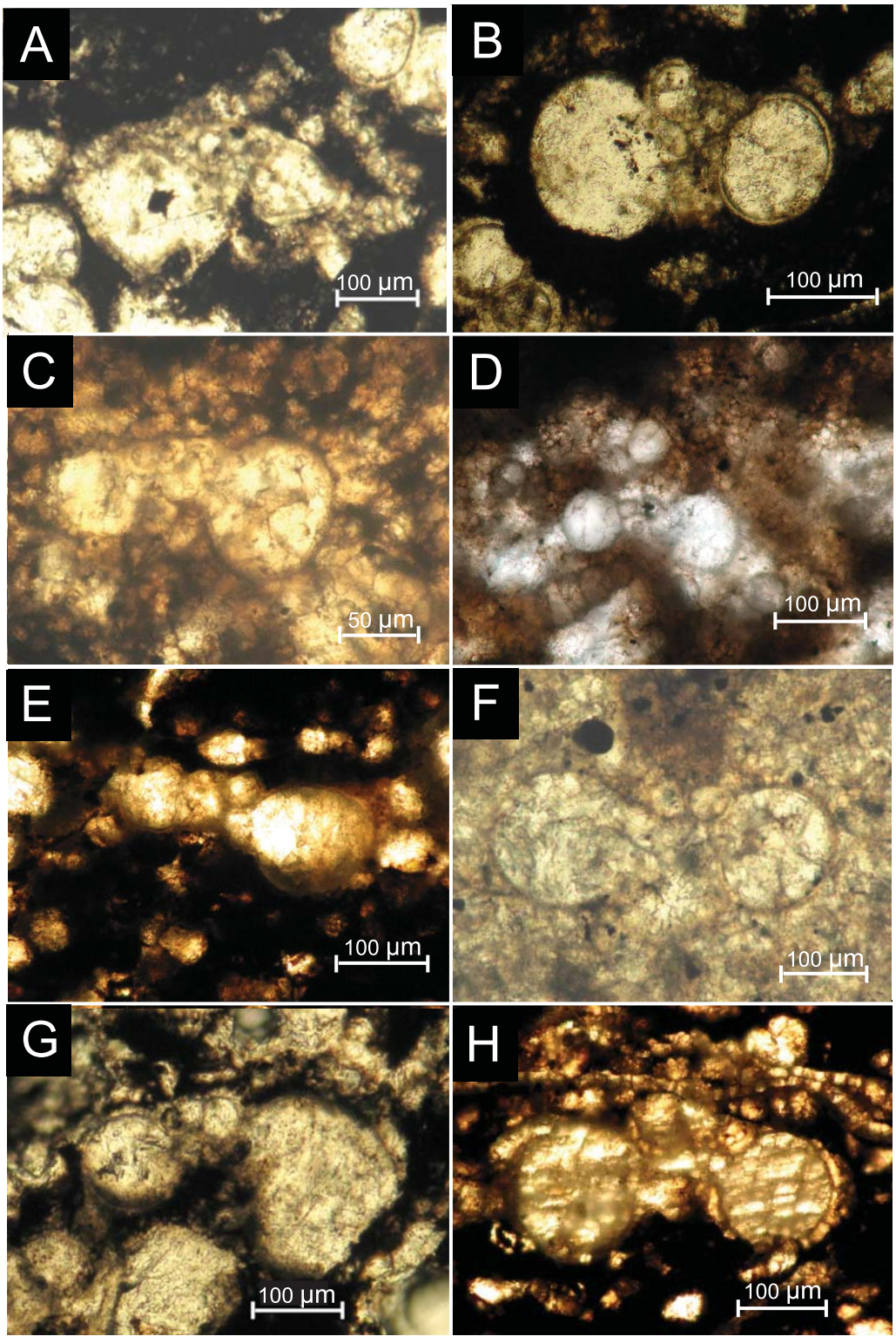

Figure 4 Continued

(Double column-full page width)

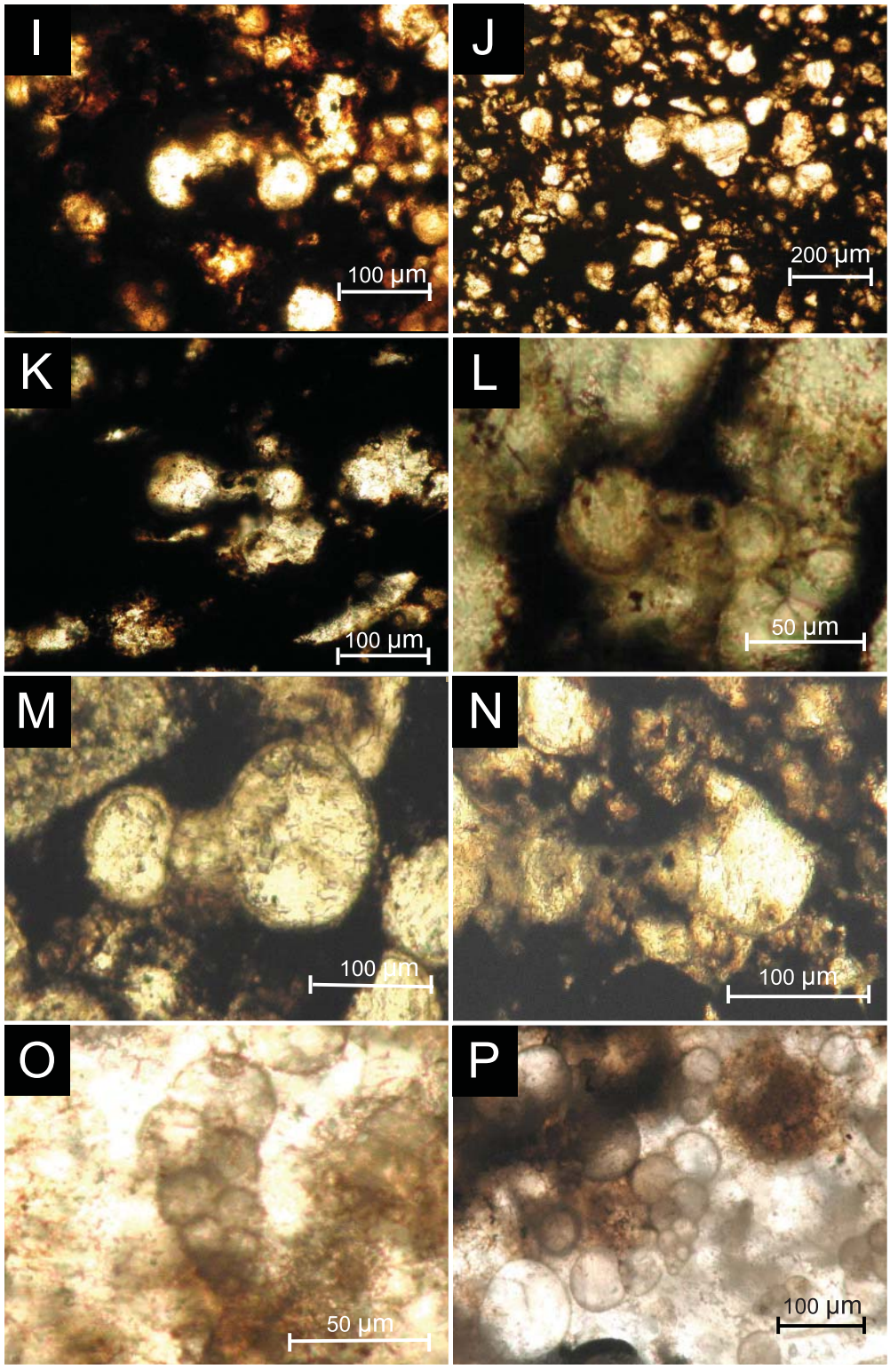

Figure 5

(Double column-full page width)

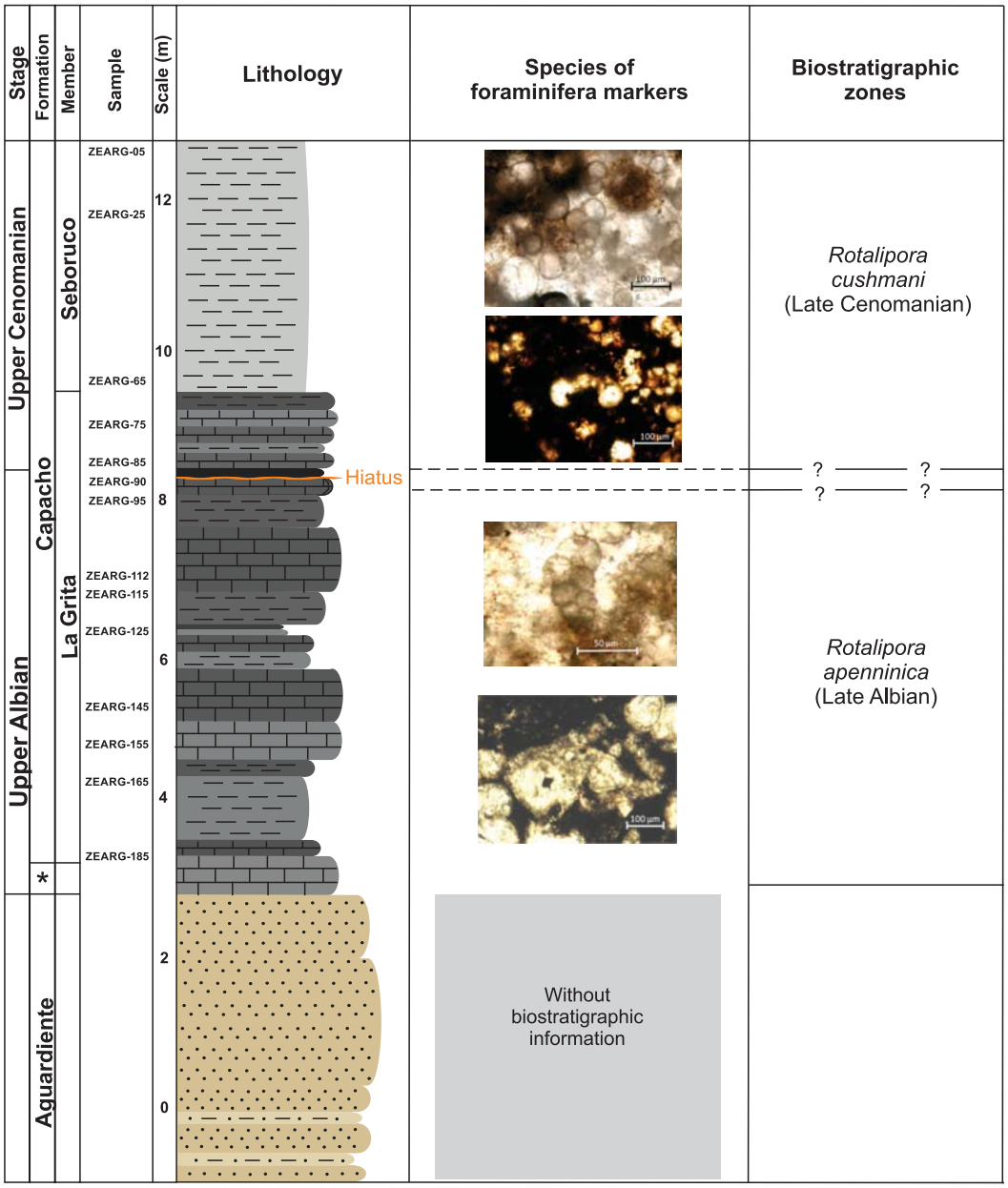

* **Maraca**

Legend

- Limestone (with high content of organic matter)
- Calcareous shale (with high content of organic matter)
- Sandstone
- Siltstone

Figure 6

(double column-full page width)

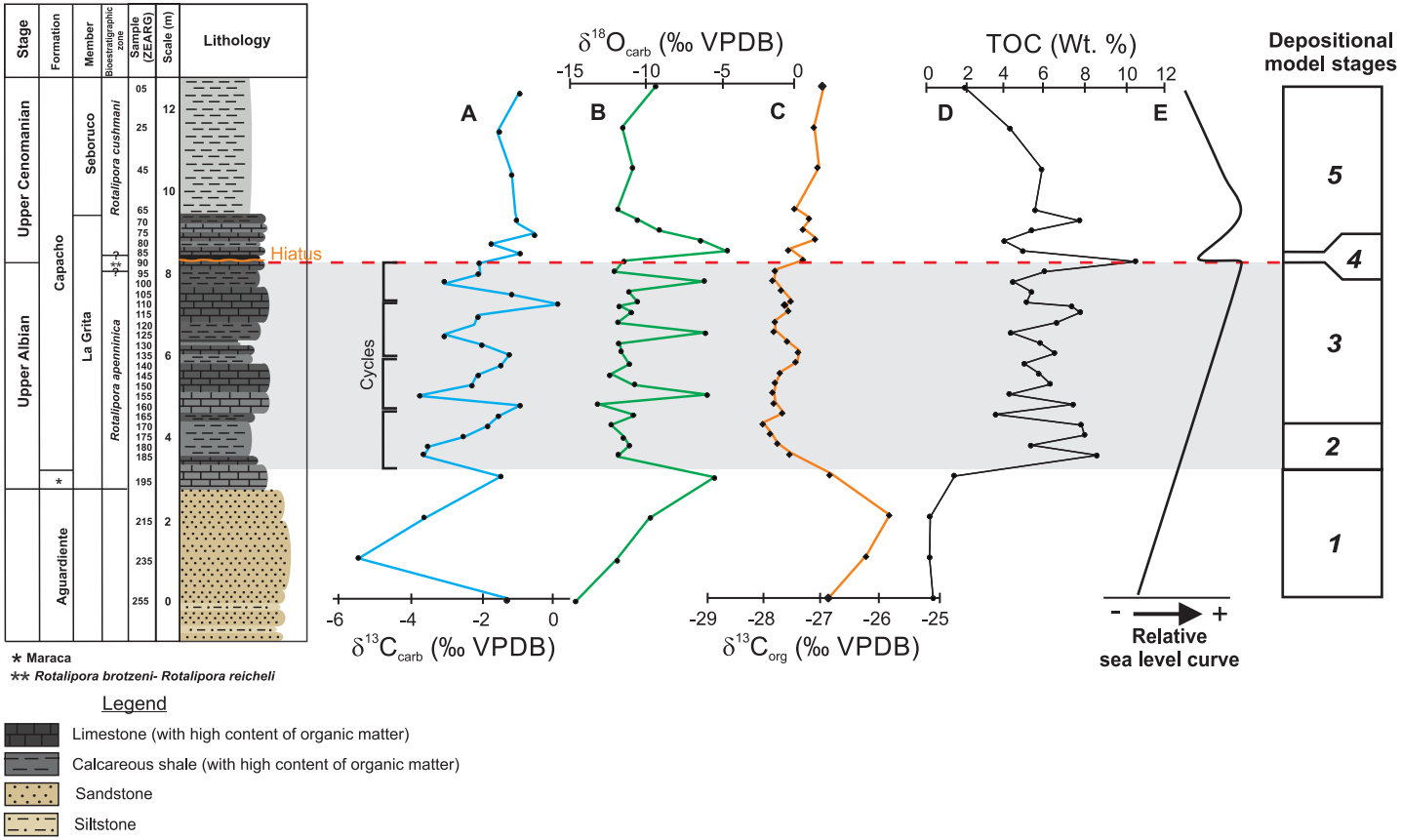

Figure 7

(Double column-full page width)

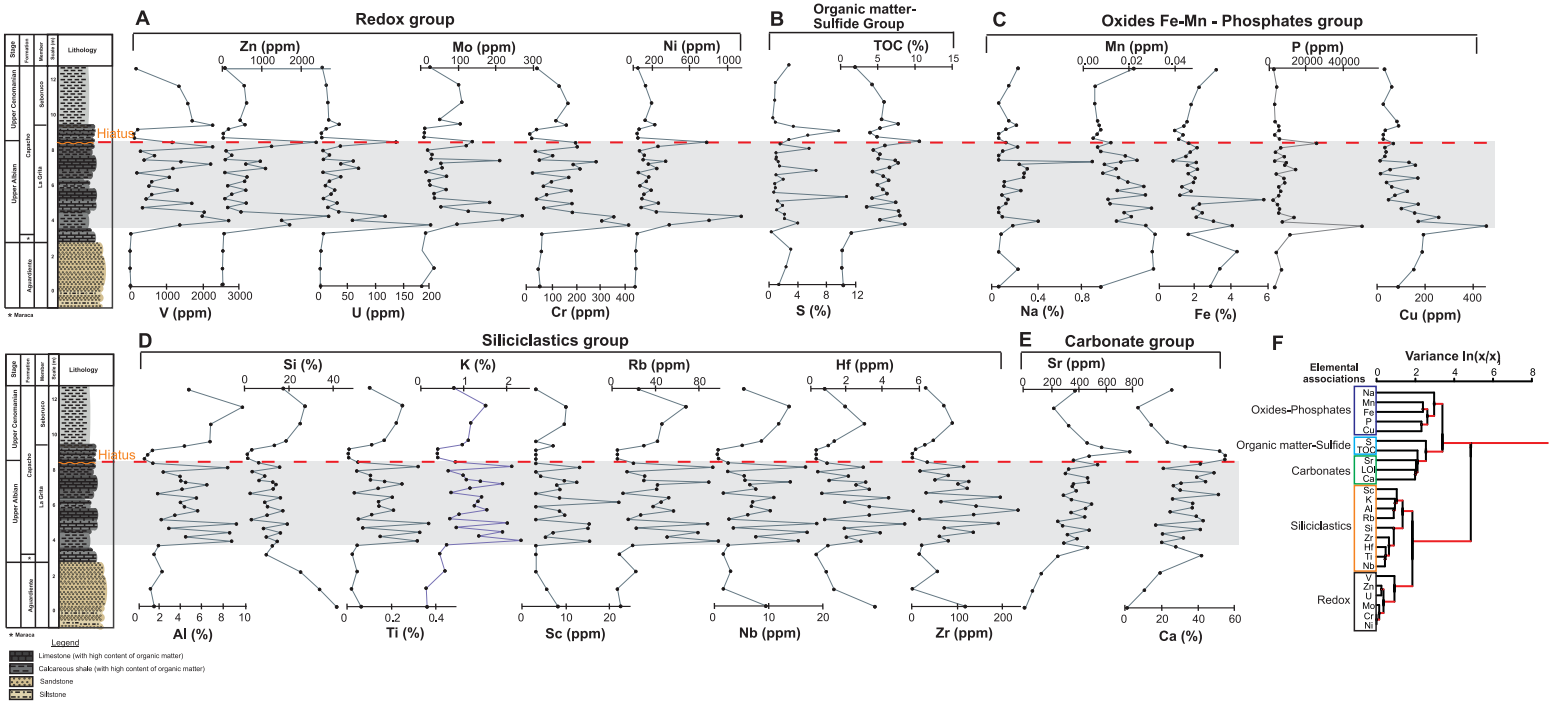

Figure 8

(Double column full page with)

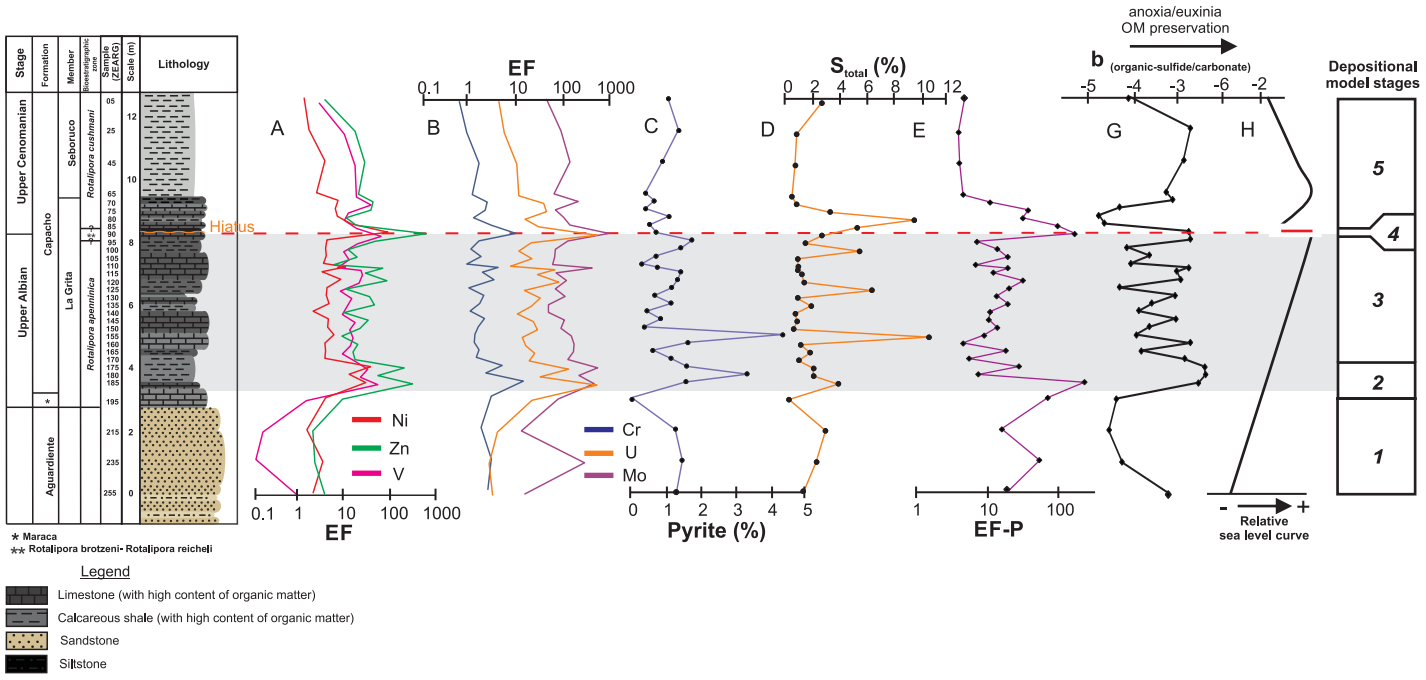

Figure 9
(Single column)

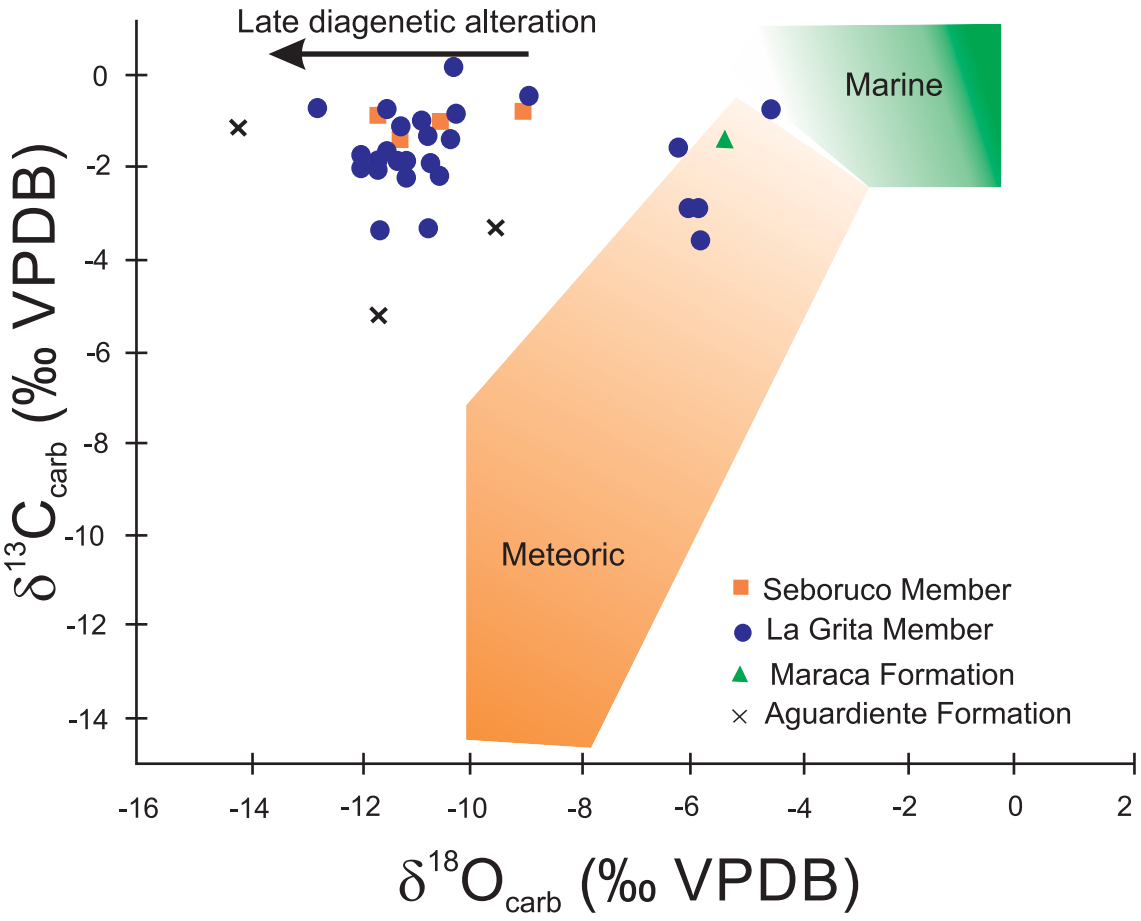

Figure 10

(Double column- full page width)

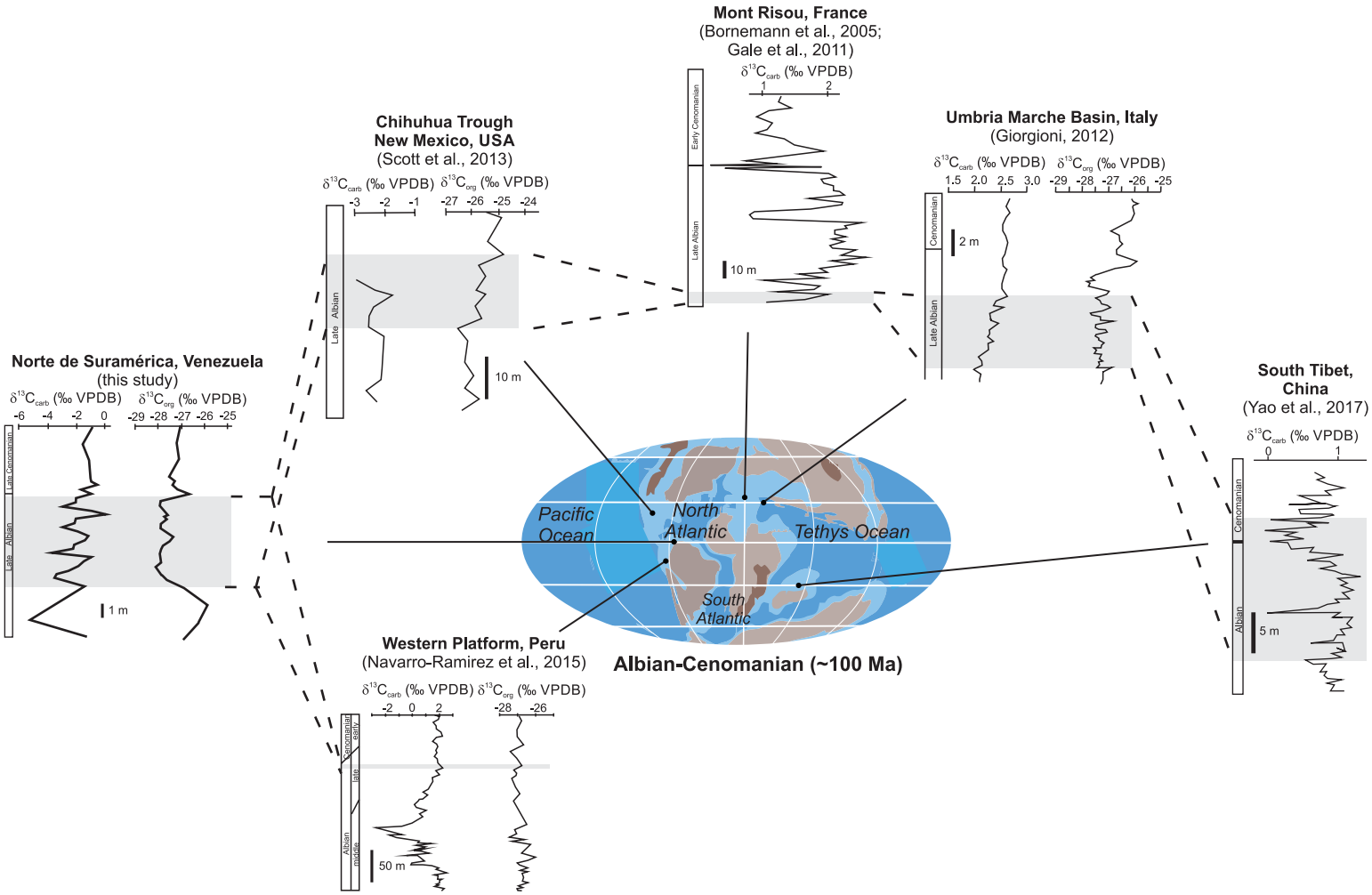

Figure 11
(double column)

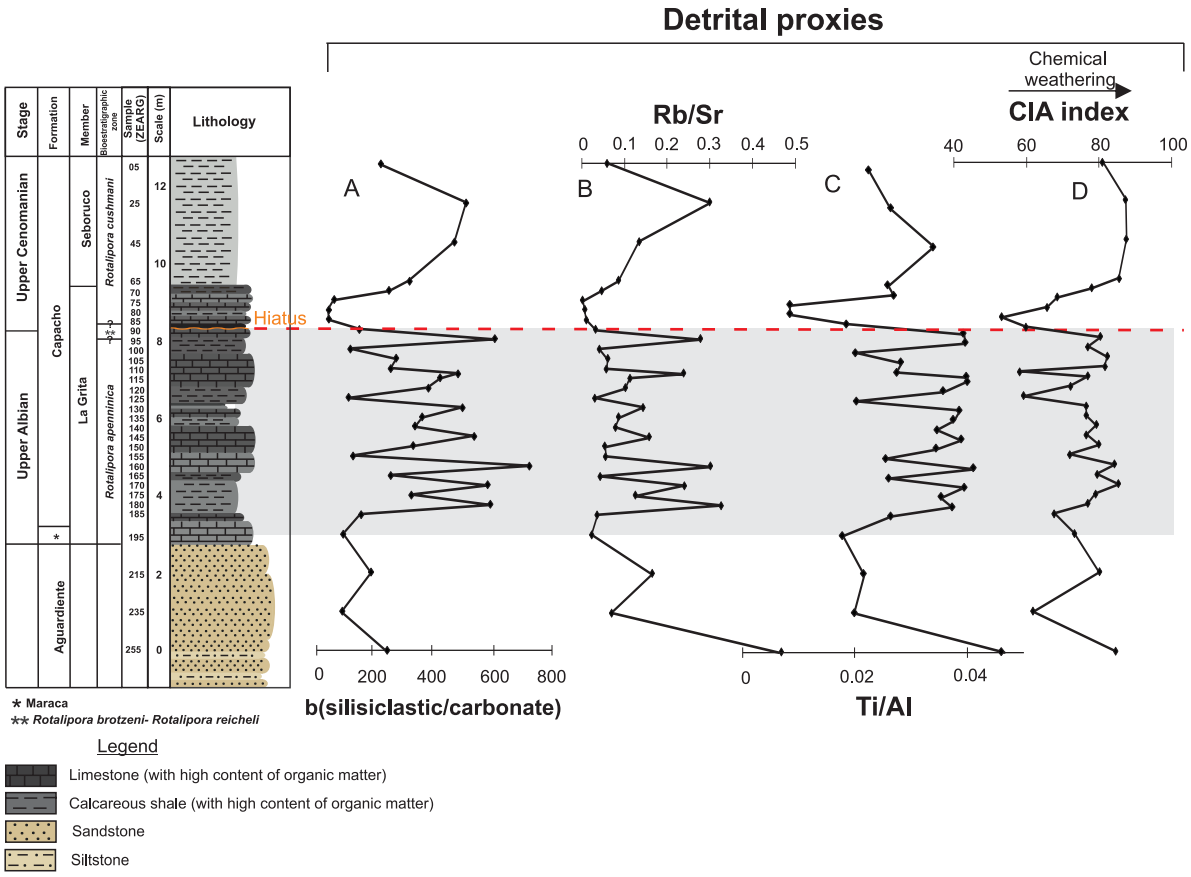

Figure 12

(Single column)

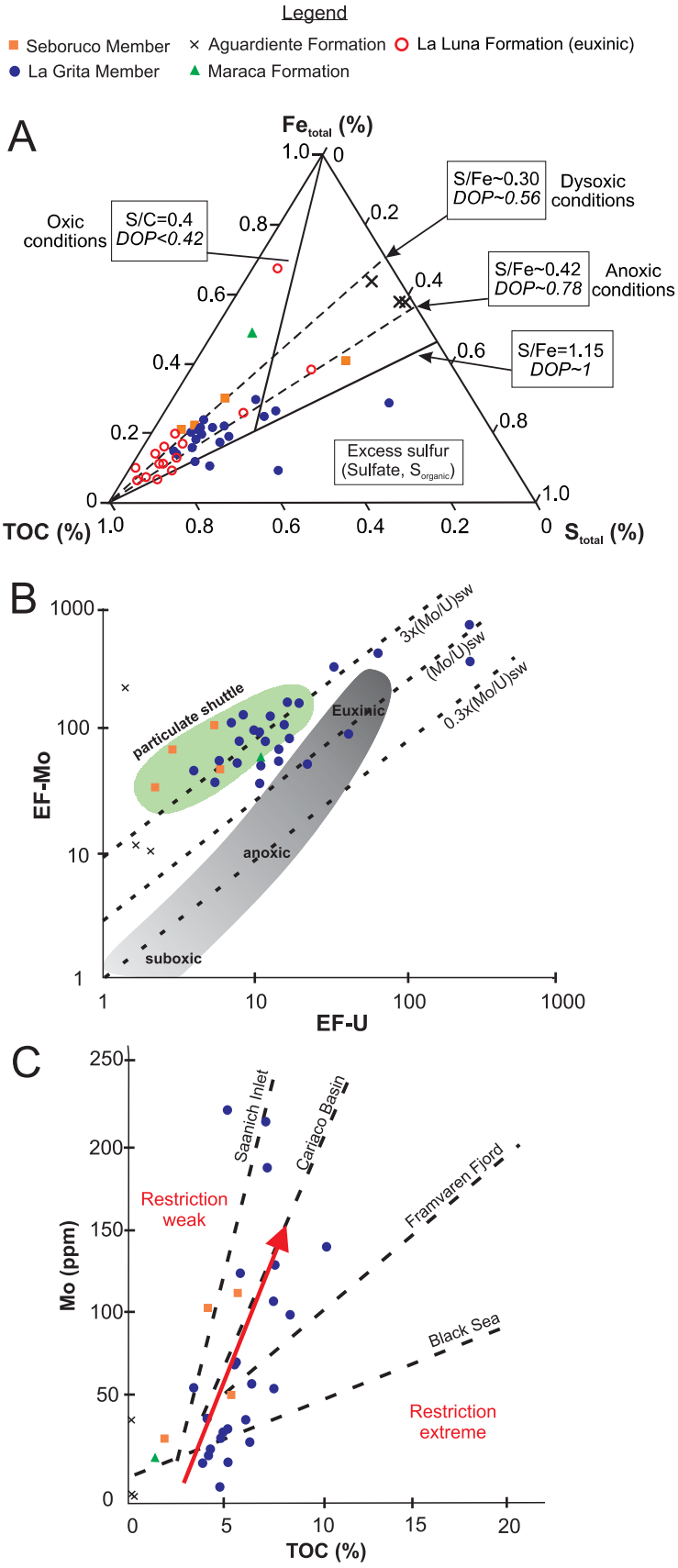

Figure 13
(Double column- full page width)

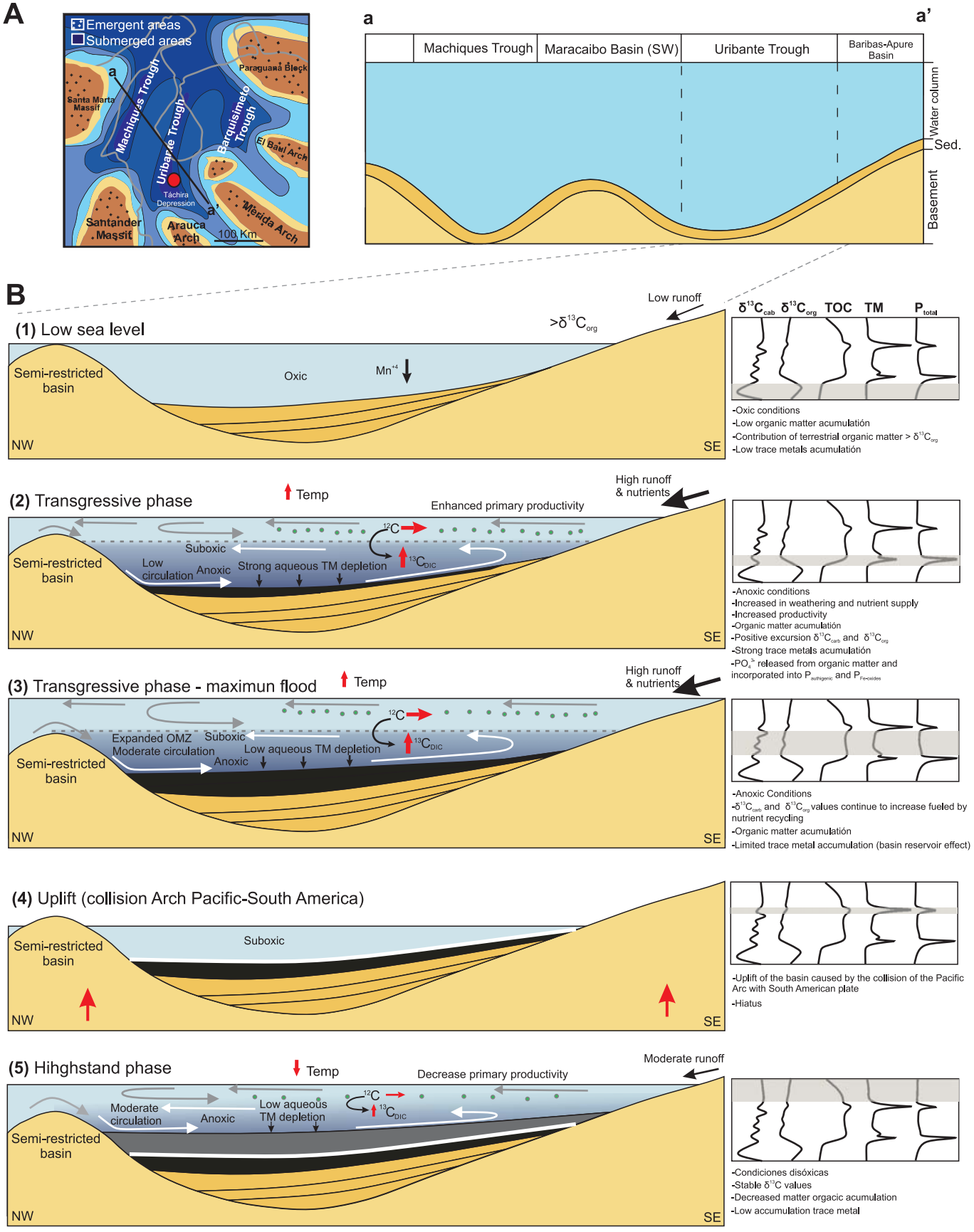

Appendix A

Appendix A.1. Analytical results of isotopic concentrations in CAL-INT (in-house standard) determined by IRMS . SD: standard deviation; RD: relative deviation to reference values; RSD: relative standard deviation (1σ).

Sample-ID	$\delta^{13}C_{(VPDB)}$	$\delta^{18}O_{(VPDB)}$
	‰	
CAL-INT	-1.52	-7.8
CAL-INT	-1.57	-8.0
CAL-INT	-1.50	-7.9
CAL-INT	-1.56	-7.9
CAL-INT	-1.73	-8.4
CAL-INT	-1.48	-7.9
CAL-INT	-1.52	-8.0
CAL-INT	-1.77	-8.4
CAL-INT	-1.77	-8.3
CAL-INT	-1.57	-7.8
CAL-INT	-1.56	-7.8
CAL-INT	-1.57	-7.9
CAL-INT	-1.64	-8.0
CAL-INT	-1.64	-8.1
CAL-INT	-1.62	-8.0
CAL-INT	-1.55	-7.9
CAL-INT	-1.50	-7.8
Median	-1.59	-8.0
SD	0.09	0.2
Ref. values CAL-INT	-1.59 ± 0.03	-8.0 ± 0.1
RD	1	1
RSD	5.66	2.5

Appendix A.2. Analytical results of isotopic concentrations in Acetanilide and Sucrose (in-house standard) determined by EA connected to IRMS. SD: standard deviation; RD: relative deviation to reference values; RSD: relative standard deviation (1σ).

	Acetanilide	**Sucrose**
	$\delta^{13}C$ ‰	
	-30.65	-11.7
	-30.63	-12.0
	-30.66	-12.2
	-30.69	-11.8
	-30.64	-12.1
	-30.66	-11.6
Median	-30.66	-11.9
SD	0.02	0.2
Ref. values	-30.66	-11.9
RD	1	1
RSD	0.06	2.05

Appendix A.3. Carbon and oxygen isotopic values of certified reference materials used in this study to prepare external calibration.

Standard-ID	**$\delta^{13}C_{(VPDB)}$**	**$\delta^{18}O_{(VPDB)}$**	Reference
NSB16	-41.61 ± 0.03	-36.09 ± 0.01	Coplen and Kendall, 1982
NSB17	-4.48 ± 0.02	-18.71 ± 0.04	Coplen and Kendall, 1982
NSB18	-5.01 ± 0.06	-23.00 ± 0.06	Stichler, 1995
NSB19	+1.95	-2.20	Hut, 1987
NSB22	-29.74 ± 0.12		Gonfiantini et al.,1995
USG24	-15.99 ± 0.25		Stichler, 1995

Coplen, T.B., Kendall, C., 1982. Preparation and stable isotope determination of NBS-16 and NBS-17 carbon dioxide reference samples. Analytical Chemistry 54, 2611-2612.

Gonfiantini, R., Stichler, W., and Rozanski, K., 1995, Standards and intercomparison materials distributed by the International Atomic Energy Agency for stable isotope measurements, in Reference and intercomparison materials for stable isotopes of light elements: Vienna, Austria, International Atomic Energy Agency, IAEA-TECDOC-825, p. 13–29.

Hut, G., 1987, Consultants' group meeting on stable isotope reference samples for geochemical and hydrological investigations: Vienna, International Atomic Energy Agency, 42 p.

Stichler, W., 1995, Interlaboratory comparison of new materials for carbon and oxygen isotope ratio measurements, in Reference and intercomparison materials for stable isotopes of light elements: Vienna, Austria, International Atomic Energy Agency, IAEA-TECDOC-825, p. 67–74.

Appendix B

Appendix B.1. Analytical results of majority, minority and trace elements concentrations in USGS SDC-1 certified reference material determined by energy dispersive X-ray fluorescence spectrometry (ED-XRF). SD: standard deviation; RD: relative deviation to reference values; RSD: relative standard deviation (1σ).

Sample-ID	L.O.I.	MgO	Al_2O_3	SiO_2	P_2O_5	K_2O	CaO	TiO_2	MnO	Fe_2O_3	V	Zn	Sr	Y	Zr
	%										ppm				
SDC-1	1.57	0.60	16.50	65.10	0.62	3.29	1.64	0.98	0.10	6.53	105	87	167	51	297
SDC-1	1.57	0.69	16.53	65.21	0.52	3.29	1.63	0.98	0.10	6.54	119	91	171	51	299
SDC-1	1.57	0.64	16.52	65.17	1.10	3.28	1.64	0.98	0.11	6.53	121	87	172	49	293
SDC-1	1.57	0.68	16.51	64.92	0.67	3.27	1.63	0.97	0.10	6.49	114	88	166	50	288
SDC-1	1.57	0.66	16.51	64.98	0.67	3.26	1.64	0.97	0.10	6.48	120	88	164	50	297
SDC-1	1.57	0.66	16.57	64.96	0.68	3.26	1.64	0.97	0.10	6.50	116	90	167	50	289
SDC-1	1.57	0.67	16.45	64.96	0.51	3.26	1.62	0.97	0.10	6.51	124	94	171	51	298
SDC-1	1.57	0.64	16.52	65.07	0.67	3.29	1.63	0.97	0.10	6.52	112	92	169	52	295
Median	1.57	0.66	16.52	65.03	0.67	3.28	1.63	0.97	0.10	6.51	118	89	168	50	296
SD		0.03	0.03	0.11	0.18	0.01	0.01	0.00	0.00	0.02	6.11	2.73	2.62	0.94	4.10
Ref. values SDC-1		1.69 ± 0.10	16.1 ± 0.34	66.7 ± 0.4	0.16 ± 0.03	3.28 ± 0.10	1.4 ± 0.07	1.01 ± 0.04	0.11 ± 0.01	6.8 ± 0.23	102	103	171	40	290
RD		0.39	1.03	0.97	4.16	1.00	1.17	0.96	0.94	0.96	1.15	0.87	0.98	1.26	1.02
RSD		4.19	0.21	0.16	27.69	0.41	0.46	0.34	2.43	0.32	5.19	3.06	1.56	1.87	1.39

Appendix B.2. Analytical results of majority, minority and trace elements concentrations in NIST SRM 612 certified reference material determined by laser ablation inductively coupled plasma mass spectrometry (LA-ICP-MS). CaO of 11.9% was used for internal standardization. SD: standard deviation; RD: relative deviation to reference values; RSD: relative standard deviation (1σ).

Sample-ID	Na_2O	Al_2O_3	Sc	Cr	Co	Ni	Cu	Zn	Rb	Y	Nb	Mo	Ba	La	Ce	Pr	Nd	Sm	Eu	Gd	Tb	Dy	Ho	Er	Tm	Yb	Lu	Hf	Th	U
	%		ppm																											
NIST 612	13.1	1.99	42.7	40	34.9	37.5	35.8	38.8	31.7	38	38.9	38	37.6	35.8	38.1	37.4	35.4	36.7	34.5	36.4	35.8	35.1	37.4	37.5	37	39.8	37.6	33.7	37.8	37.2
NIST 612	13.6	2.01	39.7	40.1	35.9	39.7	37.9	37.3	31.8	38.8	37.6	38.9	38.2	36.1	38.9	37.3	35.3	37.1	34.7	37.9	36.4	37.1	38.6	37.7	38.4	40.4	38.2	36.2	37	37.4
NIST 612	13.6	1.93	39.1	41.4	36.6	39.6	38.3	40.2	32.7	34.4	38.1	39.4	38.8	35.3	39.1	38	35.8	35.9	34.1	34.5	33.7	33.5	35	35	34.5	37.6	34.4	31.8	35.4	38
NIST 612	13.1	2.06	43.3	38.7	34.2	37.6	35.4	36	30.9	42.5	38.4	37.5	37	36.5	38	36.7	35	37.9	35.1	39.7	38.4	38.8	41.1	40.2	41	42.7	41.3	38	39.4	36.6
NIST 612	13.3	2	40.8	40.9	35.3	38.6	36.7	37.3	31.8	38.5	38.2	38.3	38	35.9	38.1	36.8	35.2	37.1	34.1	37.1	36	36	37.9	37.4	37.4	39.9	37.7	34.9	37.2	36.7
NIST 612	13.5	1.99	41.6	39.2	35.5	38.6	37	38.8	31.7	38.3	38.2	38.6	37.8	36	38.9	37.9	35.6	36.7	35.1	37.2	36.1	36.3	38.2	37.8	38	40.3	38	35	37.6	37.9
NIST 612	13.5	2.01	40.4	39.1	34.7	38.5	37.9	38.8	31.6	38.2	37.9	37.8	37.8	36	38.4	37.1	35.2	36.9	34.4	36.5	35.5	35.9	37.8	37.3	37.8	40.3	37.9	35.1	37.2	37.4
NIST 612	13.3	1.99	42	41	36.1	38.7	35.8	37.4	32	38.7	38.6	39.2	38	35.8	38.6	37.5	35.6	36.8	34.8	37.7	36.6	36.3	38.2	37.9	37.6	39.9	37.9	34.7	37.6	37.2
NIST 612	13.4	2.01	41.1	39	35.1	38.5	37.1	37.5	31.7	38.2	37.2	37.9	37.8	35	37.1	37	34.6	35.9	34.8	36.6	35.1	35.3	37.3	36.9	37.5	39.9	37.5	34.6	36.7	36.5
NIST 612	13.3	1.98	41.3	41.1	35.7	38.8	36.6	38.7	31.8	38.7	39.2	39	38	36.8	40	37.6	36.2	37.9	34.4	37.6	37	37	38.8	38.3	37.9	40.3	38.2	35.3	38.1	38.1
NIST 612	13.3	2	40.5	39.6	35.1	38.3	37.3	37.7	31.5	38	38	38.4	37.7	36.2	39	37.6	35.5	36.8	34.2	36.5	35.8	35.5	38	37.1	37.6	40.5	37.9	34.6	37	37
NIST 612	13.5	2	41.9	40.5	35.7	38.9	36.4	38.5	32	38.8	38.4	38.5	38.1	35.7	38.1	37	35.3	37	35	37.7	36.4	36.7	38.1	38.1	37.8	39.7	37.9	35.2	37.7	37.6
Mediane	13.4	2.0	41.2	40.1	35.4	38.6	36.9	38.1	31.8	38.4	38.2	38.5	37.9	36.0	38.5	37.4	35.4	36.9	34.6	37.2	36.1	36.2	38.1	37.6	37.7	40.1	37.9	35.0	37.4	37.3
SD	0.17	0.03	1.20	0.93	0.66	0.65	0.91	1.09	0.41	1.75	0.54	0.59	0.42	0.48	0.73	0.42	0.40	0.62	0.37	1.23	1.12	1.29	1.37	1.18	1.43	1.12	1.49	1.44	0.94	0.54
Ref. values NIST 612	13.3	1.99	41.1	39.9	35.3	38.4	36.7	37.9	31.6	38.3	38.1	38.3	37.7	35.8	38.4	37.2	35.2	36.7	34.4	37	35.9	36	37.9	37.4	37.6	40	37.7	34.8	37.2	37.2
RD	1.0	1.0	1.0	1.0	1.0	1.0	1.0	1.0	1.0	1.0	1.0	1.0	1.0	1.0	1.0	1.0	1.0	1.0	1.0	1.0	1.0	1.0	1.0	1.0	1.0	1.0	1.0	1.0	1.0	1.0
RSD	1.3	1.5	2.9	2.3	1.9	1.7	2.5	2.9	1.3	4.6	1.4	1.5	1.1	1.3	1.9	1.1	1.1	1.7	1.1	3.3	3.1	3.6	3.6	3.1	3.8	2.8	3.9	4.1	2.5	1.4

Appendix C

Appendix C.1. Concentration of the majority, minority and trace elements for the total samples analyzed.

Sample-ID	Al*	Si *	P *	K*	Ca*	Na *	Ti*	Mn*	Fe*	V*	Sr*	Zr*	Sc**	Cr**	Ni**	Cu**	Zn**	Rb**	Mo**	Hf**	Th**	U**
				%						ppm												
ZEARG-05	4.61	17.75	0.23	0.76	25.59	0.24	0.10	0.02	3.14	172.8	387.0	32.7	3.28	45.40	51.00	31.00	63.80	24.50	24.70	0.77	7.58	4.23
ZEARG-25	9.61	27.78	0.40	1.49	6.99	0.16	0.25	0.01	2.18	1350	223.9	74.4	10.20	137.00	134.00	60.50	585.00	68.10	104.00	1.89	17.10	11.50
ZEARG-45	6.65	25.51	0.29	1.15	14.31	0.06	0.23	0.01	1.76	1600	332.4	93.7	9.81	173.00	201.00	25.10	645.00	45.80	113.00	2.95	12.80	14.70
ZEARG-65	6.58	19.03	0.32	1.09	23.20	0.16	0.17	0.01	1.52	1720	467.6	49.9	3.28	123.00	131.00	82.50	475.00	41.90	51.10	1.30	11.20	16.10
ZEARG-70	4.22	13.69	0.50	0.95	32.90	0.23	0.11	0.01	1.35	2280	575.1	31	7.20	166.00	237.00	88.90	604.00	29.40	108.00	0.97	6.39	34.80
ZEARG-75	1.25	3.32	0.53	0.39	51.85	0.13	0.01	0.01	0.84	211.9	781	9.9	3.28	44.00	63.10	33.20	164.00	5.03	10.30	0.30	1.05	11.70
ZEARG-80	0.79	1.25	0.28	0.38	55.01	0.06	0.01	0.01	1.31	108.6	483.9	2.475	3.28	16.00	43.60	26.00	30.30	5.03	10.00	0.30	0.58	2.63
ZEARG-85	0.48	1.52	0.55	0.39	54.66	0.06	0.01	0.00	1.07	121.3	368.2	2.475	3.28	23.00	51.10	25.70	30.30	5.03	8.20	0.30	0.69	3.15
ZEARG-90	1.27	6.53	2.59	0.80	41.26	0.13	0.05	0.01	1.62	1170	543.8	35.8	3.28	204.00	808.00	67.50	2500.00	19.90	141.00	0.90	5.38	139.00
ZEARG-95	8.22	16.21	0.63	2.08	20.99	0.24	0.33	0.01	2.08	2280	331.0	119.5	13.30	212.00	273.00	32.10	1310.00	93.00	125.00	2.88	20.00	37.10
ZEARG-100	2.24	3.60	0.34	0.63	48.86	0.10	0.056	0.01	1.70	296.6	308.9	19.6	3.28	38.80	69.30	36.70	97.30	13.80	18.30	0.39	3.13	5.47
ZEARG-105	3.80	9.32	0.81	0.97	39.27	0.06	0.11	0.02	1.45	677.5	470.0	84.3	4.37	110.00	121.00	32.60	254.00	30.20	30.50	2.06	7.74	17.50
ZEARG-110	3.89	6.64	0.29	1.05	44.25	0.06	0.11	0.02	0.75	390.5	476.3	53.7	9.78	54.60	108.00	11.60	81.70	29.40	28.50	1.00	6.68	6.45
ZEARG-112	4.32	12.94	0.94	1.36	30.78	0.92	0.17	0.02	2.03	1410	368.3	130.9	12.70	290.00	354.00	132.00	1010.00	89.20	217.00	3.02	17.50	60.80
ZEARG-115	6.30	14.38	0.84	1.88	26.40	0.25	0.25	0.01	1.56	2220	360	106	8.06	195.00	167.00	159.00	625.00	42.00	55.00	2.48	9.18	38.10
ZEARG-120	4.01	13.25	1.45	1.12	30.22	0.33	0.14	0.01	2.09	1190	387.6	127.6	8.78	223.00	260.00	53.20	1150.00	41.00	57.90	3.23	12.00	70.50
ZEARG-125	1.71	2.52	0.39	0.69	51.19	0.30	0.03	0.01	1.59	196.9	294.4	33.9	3.28	27.00	55.90	13.40	65.90	10.20	14.40	0.60	2.15	5.49
ZEARG-130	5.33	16.48	0.80	1.39	26.14	0.29	0.21	0.02	1.97	1090	354.2	202.7	8.71	177.00	170.00	168.00	659.00	52.40	71.00	4.29	12.10	38.00
ZEARG-135	3.83	9.28	0.84	1.31	37.05	0.12	0.14	0.02	1.88	602	501.0	67.8	22.30	105.00	142.00	38.80	599.00	45.10	22.50	1.87	9.89	17.40
ZEARG-140	4.23	10.63	0.51	1.23	36.90	0.11	0.15	0.03	1.23	528.6	456.0	147.5	3.28	71.20	70.80	60.70	148.00	37.70	24.90	3.23	7.39	9.68
ZEARG-145	5.45	17.54	0.62	1.52	24.79	0.27	0.21	0.02	1.74	1310	349.6	243.1	8.71	187.00	195.00	126.00	626.00	56.50	69.60	5.63	12.20	27.00
ZEARG-150	3.31	10.37	0.50	0.88	38.99	0.09	0.11	0.03	1.14	603.9	449.9	141.8	9.87	84.50	115.00	74.10	248.00	26.30	36.10	3.22	6.71	20.10
ZEARG-155	2.07	3.15	0.20	0.66	42.85	0.15	0.05	0.01	5.78	451.7	252.8	18.7	3.28	44.10	95.60	46.90	65.20	15.10	36.80	0.76	3.41	6.08
ZEARG-160	9.05	19.66	0.44	1.98	16.66	0.13	0.37	0.01	2.21	1710	288.4	198	15.50	190.00	275.00	170.00	633.00	88.10	189.00	5.16	22.50	31.50
ZEARG-165	2.76	8.79	0.56	0.81	41.36	0.06	0.07	0.03	1.86	350.6	482.5	74.7	15.20	73.50	85.70	101.00	148.00	22.40	55.50	1.85	7.47	14.70
ZEARG-170	8.42	16.50	0.50	1.87	20.60	0.06	0.33	0.02	2.36	2050	324.5	141.6	7.20	192.00	256.00	155.00	500.00	79.20	130.00	3.81	23.10	34.70
ZEARG-175	4.32	10.07	1.35	1.33	32.04	0.10	0.15	0.02	2.04	1990	393.4	63.5	5.45	362.00	1190.00	254.00	2830.00	50.70	279.00	1.95	19.10	119.00
ZEARG-180	8.61	15.08	0.70	2.30	19.98	0.43	0.32	0.02	2.98	2720	296.4	83.9	15.60	313.00	833.00	170.00	1580.00	98.00	224.00	2.75	23.20	59.60
ZEARG-185	1.80	12.80	5.09	0.59	27.87	0.19	0.05	0.03	4.02	1370	471.4	23.8	3.28	425.00	394.00	451.00	1790.00	18.90	99.80	0.93	11.40	202.00

ZEARG-195	1.37	9.98	1.14	0.43	41.85	0.09	0.02	0.03	1.59	27.6	253	17.9	3.28	65.60	42.50	192.00	45.00	6.71	12.90	0.30	2.41	6.34
ZEARG-215	2.15	25.71	0.38	0.55	19.16	0.06	0.05	0.03	4.28	4.6	130.7	58.8	3.28	63.10	26.90	186.00	16.40	22.00	3.45	0.85	3.63	1.84
ZEARG-235	1.06	34.57	0.66	0.13	10.57	0.24	0.02	0.03	3.33	1.5	68.4	2.475	5.70	50.90	29.30	151.00	8.97	5.03	36.00	1.28	2.39	0.62
ZEARG-255	1.39	42.36	0.30	0.15	1.17	0.06	0.06	0.01	2.83	17.3	17.1	123.2	8.31	57.50	23.30	86.30	19.00	7.97	2.59	3.53	4.52	0.97

* obtained by energy dispersive X-ray fluorescence spectrometry

** obtained by laser ablation inductively coupled plasma mass spectrometry

Appendix C.2. Isotope compositions, total organic carbon (TOC), total sulfur (S_{total}) and pyrite (%) content for the total samples analyzed.

Sample-ID	**$\delta^{13}C$ $CaCO_3$ (VPDB) ± 0.20‰**	**$\delta^{18}O$ $CaCO_3$ (VPDB) ± 0.5‰**	**$\delta^{13}Corg$ (VPDB) ± 0.10‰**	**TOC (%)**	**S_{total} (%)**	**Pyrite (%)**
ZEARG-05	-0.86	-9.0	-27.04	1.93	2.74	1.04
ZEARG-25	-1.49	-11.2	-27.19	4.22	0.88	1.34
ZEARG-45	-1.09	-10.5	-27.11	5.83	0.78	0.88
ZEARG-65	-0.99	-11.5	-27.51	5.49	0.53	0.39
ZEARG-70	-0.93	-10.2	-27.27	7.74	0.89	0.64
ZEARG-75	-0.46	-8.8	-27.38	5.31	3.38	0.39
ZEARG-80	-1.66	-6.1	-27.16	3.93	9.65	1.06
ZEARG-85	-0.86	-4.4	-27.62	4.88	5.38	0.51
ZEARG-90	-1.97	-11.1	-27.36	10.57	2.75	0.70
ZEARG-95	-1.96	-11.7	-27.85	5.97	1.53	1.72
ZEARG-100	-2.95	-5.9	-27.89	4.37	5.55	1.41
ZEARG-105	-1.08	-10.8	-27.74	5.30	0.95	0.69
ZEARG-110	0.19	-10.2	-27.59	5.06	1.02	0.29
ZEARG-112	-0.83	-11.4	-27.68	7.33	0.96	0.73
ZEARG-115	-2.00	-10.6	-27.63	7.76	1.27	1.41
ZEARG-120	-2.10	-11.5	-27.86	6.58	1.43	1.31
ZEARG-125	-2.92	-5.8	-27.87	4.28	6.49	1.15
ZEARG-130	-1.83	-11.4	-27.65	5.76	0.96	0.65
ZEARG-135	-1.16	-11.2	-27.46	6.48	1.96	1.13
ZEARG-140	-1.38	-10.7	-27.50	4.93	0.80	0.43
ZEARG-145	-2.05	-11.9	-27.77	5.69	0.90	0.83
ZEARG-150	-2.18	-10.5	-27.85	6.26	0.66	0.35
ZEARG-155	-3.67	-5.7	-27.90	4.20	10.75	4.32
ZEARG-160	-0.84	-12.7	-27.88	7.41	1.20	1.61
ZEARG-165	-1.46	-10.3	-27.73	3.49	1.90	1.61
ZEARG-170	-1.75	-11.9	-28.07	7.82	1.05	1.13
ZEARG-175	-2.38	-11.1	-27.94	7.98	2.13	1.57
ZEARG-180	-3.34	-10.7	-27.82	5.28	2.13	3.3
ZEARG-185	-3.49	-11.5	-27.60	8.63	3.98	1.55
ZEARG-195	-1.38	-5.2	-26.90	1.41	0.32	---
ZEARG-215	-3.43	-9.5	-25.89	0.19	3.03	1.25
ZEARG-235	-5.28	-11.5	-26.29	0.16	2.35	1.44
ZEARG-255	-1.22	-14.1	-26.92	0.33	1.36	1.28